Styxl2 regulates de novo sarcomere assembly by binding to non-muscle myosin IIs and promoting their degradation

Xianwei Chen[1†], Yanfeng Li[1†], Jin Xu[1], Yong Cui[2], Qian Wu[3], Haidi Yin[3], Yuying Li[4], Chuan Gao[1], Liwen Jiang[2], Huating Wang[4], Zilong Wen[1], Zhongping Yao[3], Zhenguo Wu[1]*

[1]Division of Life Science, Hong Kong University of Science & Technology, Hong Kong, China; [2]School of Life Sciences, Chinese University of Hong Kong, Hong Kong, China; [3]Department of Applied Biology and Chemical Technology, Hong Kong Polytechnic University, Hong Kong, China; [4]Department of Orthopaedics and Traumatology, Li Ka Shing Institute of Health Sciences, Chinese University of Hong Kong, Hong Kong, China

*For correspondence:
bczgwu@ust.hk

[†]These authors contributed equally to this work

Abstract Styxl2, a poorly characterized pseudophosphatase, was identified as a transcriptional target of the Jak1-Stat1 pathway during myoblast differentiation in culture. Styxl2 is specifically expressed in vertebrate striated muscles. By gene knockdown in zebrafish or genetic knockout in mice, we found that Styxl2 plays an essential role in maintaining sarcomere integrity in developing muscles. To further reveal the functions of Styxl2 in adult muscles, we generated two inducible knockout mouse models: one with *Styxl2* being deleted in mature myofibers to assess its role in sarcomere maintenance, and the other in adult muscle satellite cells (MuSCs) to assess its role in de novo sarcomere assembly. We find that Styxl2 is not required for sarcomere maintenance but functions in de novo sarcomere assembly during injury-induced muscle regeneration. Mechanistically, Styxl2 interacts with non-muscle myosin IIs, enhances their ubiquitination, and targets them for autophagy-dependent degradation. Without Styxl2, the degradation of non-muscle myosin IIs is delayed, which leads to defective sarcomere assembly and force generation. Thus, Styxl2 promotes de novo sarcomere assembly by interacting with non-muscle myosin IIs and facilitating their autophagic degradation.

eLife assessment

This paper presents an **important** finding: that Styxl2, a poorly characterized pseudo-phosphatase, plays a role in the sarcomere assembly by promoting the degradation of non-muscle myosins. The genetic evidence supporting the conclusions is **compelling**, although future work will be needed to elucidate the functional role and biochemical mechanism of autophagic degradation of non-muscle myosins. This work will be of interest to biologists studying muscle development, cell biology, and proteolysis.

Introduction

Striated muscles, including skeletal and cardiac muscles of vertebrates and some muscles of invertebrates, are unique in that they contain highly-organized, multi-protein contractile structures called

myofibrils in the cytosol of myofibers or cardiomyocytes (*Clark et al., 2002*; *Mukund and Subramaniam, 2020*; *Sparrow and Schöck, 2009*). Sarcomeres are the smallest repeating structural units of myofibrils responsible for muscle contraction (*Avellaneda et al., 2021*; *Squire, 2005*). A sarcomere is flanked by Z-discs (or Z lines) with multiple actin filaments (or thin filaments) anchored to the Z-discs in parallel and the interdigitating bipolar myosin bundles (or thick filaments) anchored to the M-line in the middle of the sarcomere (*Squire, 2005*). As a key component of the Z-disc, an anti-parallel α-actinin dimer directly binds to two actin filaments in opposite directions (*Squire, 2005*). A sarcomere can be further divided into the lighter I (isotropic)-band and the darker A (anisotropic)-band based on their microscopic appearances with the I-band containing actin filaments only and the A-band containing both the myosin bundles and partially overlapping actin filaments (*Craig and Padrón, 2004*; *Squire, 2005*). Mutations in sarcomeric proteins are linked to congenital human cardiac and skeletal muscle diseases (*Bönnemann and Laing, 2004*; *Parker et al., 2020*; *Parker and Peckham, 2020*). Although the overall structures of sarcomeres are well-established and the protein components of sarcomeres are largely known, it remains controversial how sarcomeres correctly assemble in vivo. Several different but not mutually exclusive models including the template model, the stitching model, and the premyofibril model have been proposed (*Martin and Kirk, 2020*; *Rui et al., 2010*; *Sanger et al., 2006*). The template model proposes that actin stress fibers serve as an early template to recruit other sarcomeric components including Z-disc proteins and the thin and thick filaments (*Dlugosz et al., 1984*). The stitching model or the titin model proposes that the actin filaments held by the Z-disc (i.e. the I-Z-I complexes) and the myosin filaments first assemble independently, and they are then stitched together to form intact sarcomeres with the help of titin as titin is known to simultaneously interact with Z-disc proteins via its N-terminal region and M-line proteins via its C-terminal region (*Holtzer et al., 1997*; *Lu et al., 1992*). The premyofibril model states that mini-sarcomeres consisting of actin filaments, α-actinin-containing Z bodies, and non-muscle myosin IIs first assemble near cell periphery. Then, non-muscle myosin IIs are replaced by muscle myosin II during the transition from premyofibrils to nascent myofibrils and finally to mature myofibrils (*Rhee et al., 1994*; *Sanger et al., 2006*). Each of these models is supported by some experimental observations but may be incompatible with others (*Chopra et al., 2018*; *Fenix et al., 2018*; *Rui et al., 2010*). In addition, mechanical tension generated by attachment of myofibers to tendon, myofiber bundling, and formation of mini-sarcomeres is also found to promote sarcomere assembly in both fly and mammalian muscle cells (*Chopra et al., 2018*; *Loison et al., 2018*; *Luis and Schnorrer, 2021*; *Mao et al., 2022*; *Weitkunat et al., 2014*).

Protein phosphatases are a family of enzymes that catalyze the removal of the phosphate group from covalently-linked substrates including proteins, lipids, nucleic acids, and polysaccharides (*Alonso et al., 2004*; *Tonks, 2006*; *Weinfeld et al., 2011*; *Worby et al., 2006*). They antagonize the actions of kinases and regulate various biological processes including tissue development, cell proliferation, differentiation, and cell migration. Interestingly, some of the protein phosphatases are found to be catalytically inactive due to the absence of essential amino acid residues such as the catalytic cysteine in an otherwise well-conserved phosphatase domain (*Chen et al., 2017*; *Reiterer et al., 2020*). These confirmed or putative catalytically inactive phosphatases are also called pseudophosphatases. Although catalytically inactive, several pseudophosphatases are found to play important roles in various organisms (*Azzedine et al., 2003*; *Cheng et al., 2009*; *Hinton, 2020*; *Reiterer et al., 2017*). For example, Styx and Sbf1, both members of the pseudophosphatase family, were found to regulate sperm development. Loss of Styx or Sbf1 resulted in male infertility in mice (*Firestein et al., 2002*; *Wishart and Dixon, 2002*).

In our current study, we identified Styxl2 (previously named as Dusp27), a poorly characterized pseudophosphatase, as a new regulator involved in sarcomere assembly in both zebrafish and mice. The original name of the gene and its protein product (i.e. Dusp27) has caused confusion in the literature due to the fact that the same name was once used for Dupd1 (now re-named as Dusp29), a catalytically active phosphatase (*Friedberg et al., 2007*). Recently, it was proposed that Dusp27 be re-named as Serine/threonine/tyrosine-interacting-like 2 (Styxl2) (*Cooper and Waddell, 2020*). To avoid further confusion, we will use Styxl2 hereafter. Styxl2 is specifically expressed in vertebrate striated muscles. Our work in both zebrafish and mouse models shows that it plays an important role in de novo sarcomere assembly instead of sarcomere maintenance. Mechanistically, we found that Styxl2 directly interacts with non-muscle myosin IIs that are involved in the early stage of sarcomere assembly and subsequently replaced by muscle myosin IIs in mature sarcomeres (*Wang et al., 2018*). Styxl2
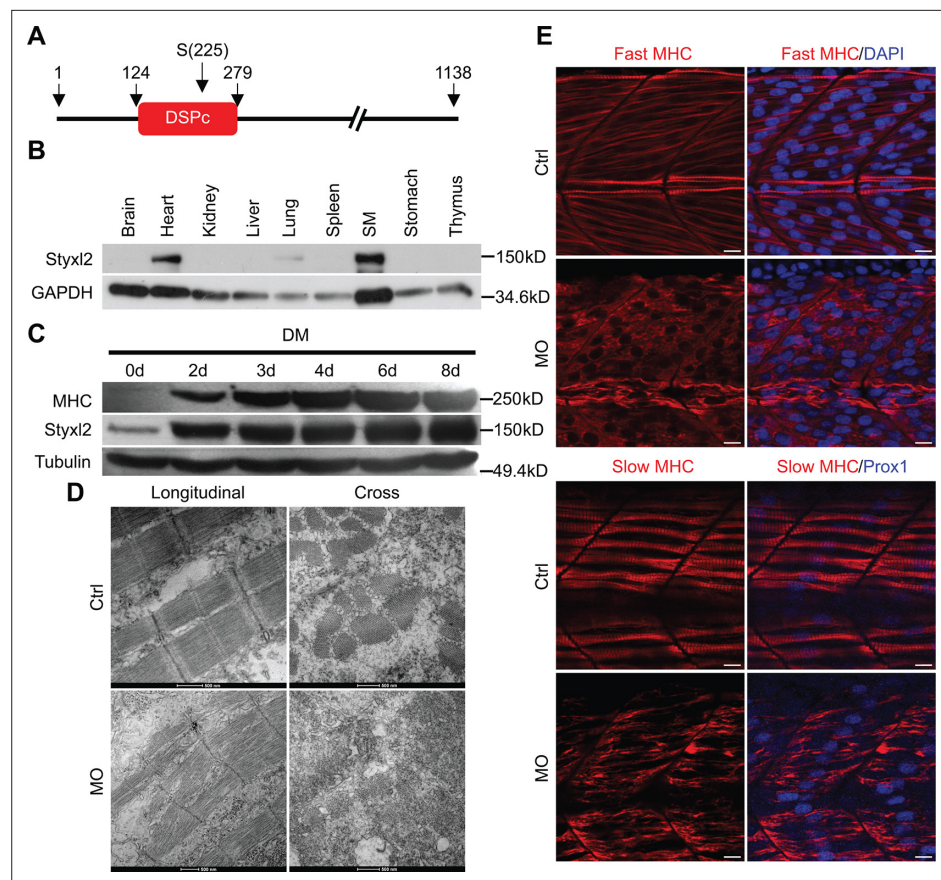
Figure 1. Styxl2 regulates sarcomere integrity during zebrafish muscle development. (**A**) A schematic of mouse Styxl2 protein. DSPc (red): dual-specificity phosphatase, catalytic domain. The numbers denote the positions of various amino acids in mouse Styxl2 including Ser (S) –225. (**B**) The expression of Styxl2 protein in different mouse tissues. 100 µg of soluble mouse tissue lysates were subjected to Western blot analysis. GAPDH: glyceraldehyde-3-phosphate dehydrogenase. SM: skeletal muscles. (**C**) The expression of Styxl2 protein in C2C12 myoblasts before and after differentiation in culture. MHC: myosin heavy chain. (**D**) Zebrafish zygotes were either mock-injected or injected with a Styxl2-specific morpholino (MO). Sarcomeres in muscles at 48 hpf were revealed by transmission electron microscopy (TEM). Representative images were shown. Scale bar: 500 nm. (**E**) Sarcomeres in fast and slow muscles of zebrafish embryos at 24 hpf were revealed by immunostaining using specific antibodies as indicated. Ctrl: control (non-treated); MO: *Styxl2*-morpholino-treated. The nuclei of slow and fast muscle fibers were counter-stained with an anti-Prox1 antibody and DAPI, respectively. Scale bar: 10 µm.

The online version of this article includes the following source data and figure supplement(s) for figure 1:

Source data 1. Original scans for the Western blot analysis in *Figure 1B* (anti-Styxl2 and anti-GAPDH).

Source data 2. A PDF file showing original scans of the relevant Western blot analysis in *Figure 1B* (anti-Styxl2 and anti-GAPDH) with highlighted bands and sample labels.

Source data 3. Original scans for the Western blot analysis in *Figure 1C* (anti-MHC, anti-Styxl2, and anti-Tubulin).

Source data 4. A PDF file showing original scans of the relevant Western blot analysis in *Figure 1C* (anti-MHC, anti-Styxl2, and anti-Tubulin) with highlighted bands and sample labels.

Figure supplement 1. Styxl2 was downstream target of Jak1-Stat1 pathway.

Figure supplement 1—source data 1. Original scans for the Western blot analysis in *Figure 1—figure supplement 1C* (anti-Jak1, anti-Stat1, anti-Styxl2, and anti-Tubulin).

Figure supplement 1—source data 2. A PDF file showing original scans of the relevant Western blot analysis in *Figure 1—figure supplement 1C* (anti-Jak1, anti-Stat1, anti-Styxl2, and anti-Tubulin) with highlighted bands and sample labels.

Figure supplement 1—source data 3. Original scans for the Western blot analysis in *Figure 1—figure supplement 1D* (anti-Styxl2).

Figure 1 continued on next page

promotes ubiquitination and autophagy-dependent degradation of non-muscle myosin IIs, which ultimately facilitates sarcomere assembly in vivo.

Results

Styxl2 encodes a striated muscle-specific pseudophosphatase and is a transcriptional target of the Jak1-Stat1 pathway in myoblasts

We previously reported that the Jak1-Stat1 pathway plays an important role in myogenic differentiation in cultured myoblasts (*Sun et al., 2007*). However, it remains unclear what genes are targeted by the pathway. To examine the changes in transcriptomes, we conducted a microarray analysis in C2C12 myoblasts: cells were first transfected with either a control siRNA or specific siRNAs targeting *Jak1* or *Stat1* and the cells were harvested at two different time points: (1) after 24 hr of growth in the growth medium (GM 24 hr, the proliferation stage); (2) after 12 hr in the differentiation medium following 24 hr of growth in the GM (DM 12 hr, the early differentiation stage). The total mRNA was extracted and subjected to microarray analysis. Among differentially expressed genes (DEGs) in cells transfected with *Jak1*-siRNA and *Stat1*-siRNA, many were shared, which was expected as both Jak1 and Stat1 function in the same pathway. Some representative targets shared by Jak1 and Stat1 were shown (*Table 1*). Consistent with our previous findings (*Sun et al., 2007*), *myogenin* gene was negatively regulated by both Jak1 and Stat1. Among the genes targeted by both Jak1 and Stat1, *serine/threonine/tyrosine-interacting-like 2* (*Styxl2*), previously also named as *dual-specificity phosphatase 27 (putative)* (*Dusp27*), attracted our attention: it is a poorly characterized gene with only one published report in zebrafish so far (*Fero et al., 2014*). It encodes a member of the dual-specificity phosphatase family with a conserved dual-specificity phosphatase catalytic (DSPc) domain located at its N-terminus (*Figure 1A*). However, Styxl2 is predicted to be catalytically inactive due to substitution of a highly-conserved catalytic cysteine by serine in its DSPc domain (*Figure 1—figure supplement 1A*), thus making it a member of the pseudophosphatase subfamily (*Hinton, 2019*; *Kharitidi et al., 2014*). By both RT-qPCR and Western blot, we confirmed that both the mRNA and protein levels of *Styxl2* were induced by siRNAs against *Jak1* or *Stat1* in C2C12 myoblasts, with the extent of induction being more obvious during early differentiation (*Figure 1—figure supplement 1B and C*). Consistently, treatment of C2C12 myoblasts with leukemia inhibitory factor (LIF) or oncostatin M (OSM), two cytokines that are known to potently activate the Jak1-Stat1 pathway in myoblasts (*Sun et al., 2007*; *Xiao et al., 2011*), indeed led to a gradual decrease of Styxl2 protein (*Figure 1—figure supplement 1D and E*). By Western blot, we found that *Styxl2* has a very limited tissue distribution pattern: it is specifically expressed in striated muscles including the heart and skeletal muscles (*Figure 1B*). Consistently, the expression of *Styxl2* mRNA is confined to the heart and somites of early mouse embryos (*Figure 1—figure supplement 1F*). In C2C12 myoblasts, Styxl2 protein was already present in proliferating myoblasts but was further induced during myogenic differentiation (*Figure 1C*). We also examined the subcellular localization of Styxl2 in myoblasts. As our home-made polyclonal antibody is not suitable for immunostaining of the endogenous Styxl2, we examined subcellular localization of Flag- or HA-tagged Styxl2 instead in C2C12 cells by immunostaining. We found that both Flag- and HA-tagged Styxl2 were predominantly localized in the cytoplasm (*Figure 1—figure supplement 1G*). Collectively, Styxl2 is a cytoplasmic protein that is specifically expressed in striated muscles.

Knockdown of *Styxl2* in zebrafish leads to severe defects in sarcomere structure

An earlier study by *Fero et al., 2014* in zebrafish showed that Styxl2 regulates the integrity of sarcomeres. We also confirmed this finding in zebrafish using a morpholino oligo (MO) that blocks the

Table 1. Candidate genes regulated by both Jak1 and Stat1.

Selected candidate genes targeted by both si-Jak1 and si-Stat1 were shown. The fold change was determined by the relative levels of a gene in cells treated with si-Jak1 or si-Stat1 over that in control cells. Genes with fold change >1.5 for si-Jak1 and >2 for si-Stat1 were listed in this table. Genes with positive fold change are up-regulated (positive value), while those with negative fold change are down-regulated (negative value). P Stage and D Stage denote the proliferation stage (growth medium. GM 24 hr) and early differentiation stage (differentiation medium, DM 12 hr), respectively.

Probe set ID	Gene	Fold change			
		P Stage		D Stage	
		siJak1	siStat1	siJak1	siStat1
1417889_at	apolipoprotein B editing complex 2	1.53	4.43	2.43	4.07
1419391_at	myogenin	4.29	9.99	2.62	4.26
1422088_at	v-myc myelocytomatosis viral oncogene homolog 1	2.12	3.9	1.88	3.68
1422606_at	C1q and tumor necrosis factor related protein 3	2.23	13.4	1.68	5.45
1426971_at	ubiquitin-activating enzyme E1-like	3.53	7.05	2.42	3.03
1427306_at	ryanodine receptor 1	2.11	6	2.71	4.52
1449178_at	PDZ and LIM domain 3	3.45	12.3	2.94	7
1451453_at	death-associated kinase 2	1.52	3.14	1.96	3.81
1452520_a_at	cholinergic receptor	6.76	15.5	2.6	4.13
1429223_a_at	hemochromatosis type 2 (juvenile) (human homolog)	2.16	28.8	2	7.66
1429459_at	sema domain	2.77	4.43	2.27	5.58
1435828_at	avian musculoaponeurotic fibrosarcoma (v-maf) AS42 oncogene homolog	1.96	3.38	1.63	3.27
1439658_at	leiomodin 3 (fetal)	1.91	17.9	2.83	18.8
1439746_at	dual specificity phosphatase 27 (putative) (dusp27)	1.82	4.78	1.73	2.36
1444494_at	kelch repeat and BTB (POZ) domain containing 10	2.46	9.63	2.79	6.38
1421426_at	Hedgehog-interacting protein	–2.04	–3.55	–1.62	–6.65
1435438_at	SRY-box containing gene 8 (sox8)	1.85	4.01	1.51	5.7

translation initiation of *Styxl2*. The effectiveness of the MO was verified using a transgene encoding green fluorescence protein (GFP) fused in-frame with the same sequence of *Styxl2* (i.e. the first 25 nucleotides of the coding region) targeted by the MO: when zebrafish zygotes were microinjected with the transgenes with or without the MO, the expression of GFP was suppressed only when the MO was co-injected (*Figure 1—figure supplement 1H*). We then injected zebrafish zygotes with or without the *Styxl2*-MO and examined the structures of skeletal muscles by immunostaining at 24 hr after fertilization (hpf). Consistent with the report by *Fero et al., 2014*, we found that sarcomeres in both fast and slow muscles were severely disrupted when *Styxl2* was knocked down with the MO (*Figure 1E*). Moreover, electron microscopy analysis further revealed the disrupted sarcomere structures in zebrafish muscles injected with the MO (*Figure 1D*).
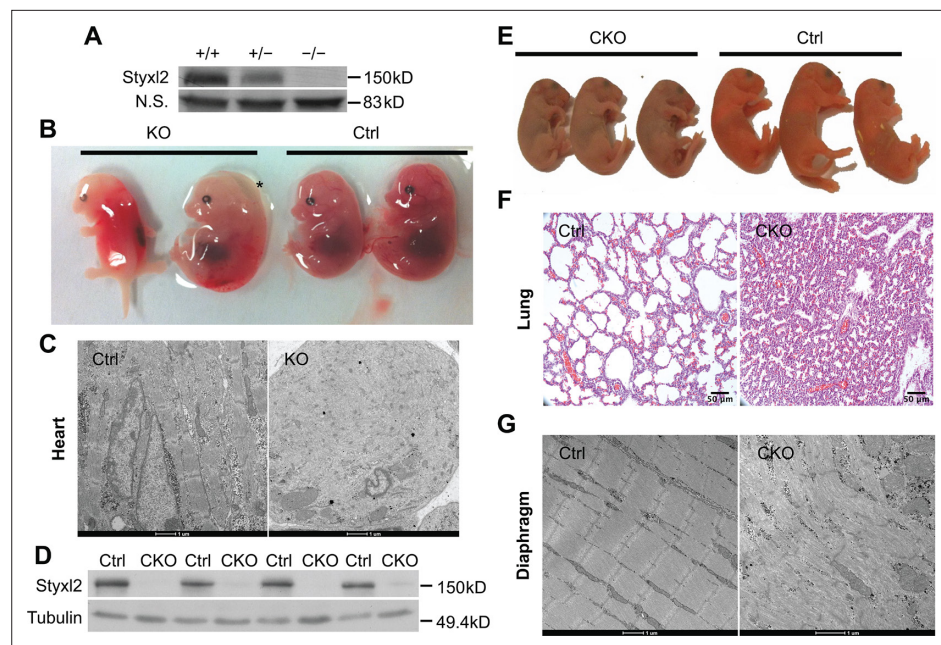
Figure 2. Conditional deletion of mouse *Styxl2* leads to defective sarcomeres in striated muscles. (**A**) The expression of Styxl2 protein in skeletal muscles of wild-type (+/+), heterozygous (+/−), and *Styxl2* knockout (KO) (−/−) (driven by *EIIA*-Cre) mice. Soluble tissue lysates from limbs of E14.5 mouse embryos were subjected to Western blot analysis. N.S.: non-specific. (**B**) E14.5 embryos of control (Ctrl) and *EIIA*-Cre; *Styxl2^{f/f}* KO mice. *: edema was found in some *Styxl2* KO foetuses. (**C**) The sarcomere structures of cardiomyocytes in the heart of E14.5 embryos from control and *EIIA*-Cre; *Styxl2^{f/f}* KO mice were revealed by transmission electron microscopy (TEM). Scale bar: 1 µm. (**D**) The expression of Styxl2 protein in skeletal muscles of control (Ctrl) and *Styxl2* CKO P1 mice. (**E**) The new-born pups (P1) from control (Ctrl) and *Pax7^{Cre/+}*; *Styxl2^{f/f}* KO mice (CKO). (**F**) Lung sections of control and Styxl2 CKO P1 mice. Scale bar: 50 µm. (**G**) The sarcomere structure of diaphragm muscles from control (Ctrl) and *Styxl2* conditional KO (CKO) P1 mice revealed by TEM. Scale bar: 1 µm.

The online version of this article includes the following source data and figure supplement(s) for figure 2:

Source data 1. Original scans for the Western blot analysis in *Figure 2A* (anti-Styxl2 and N.S.).

Source data 2. A PDF file showing original scans of the relevant Western blot analysis in *Figure 2A* (anti-Styxl2 and N.S.) with highlighted bands and sample labels.

Source data 3. Original scans for the Western blot analysis in *Figure 2D* (anti-Styxl2 and anti-Tubulin).

Source data 4. A PDF file showing original scans of the relevant Western blot analysis in *Figure 2D* (anti-Styxl2 and anti-Tubulin) with highlighted bands and sample labels.

Figure supplement 1. Both germline and conditional deletion of *Styxl2* caused lethality.

Conditional deletion of *Styxl2* leads to neonatal lethality in mutant mice

To further explore the role of Styxl2 in mammals, we generated *Styxl2* floxed mice with two LoxP sites flanking exons 3~5 of the *Styxl2* gene (*Figure 2—figure supplement 1A*). Exons 4 and 5 encode a part of the DSPc domain of Styxl2. We first generated germline *Styxl2* knockout (KO) mice using EIIA-Cre mice (*Lakso et al., 1996*). Western blot analysis showed that Styxl2 protein was totally absent in KO mice (*Figure 2A*). In multiple litters, no live homozygous KO pups were found after birth (*Figure 2—figure supplement 1B*). By examining developing embryos of different ages, we found that *Styxl2* KO embryos died between E13.5 and E15.5 (*Figure 2—figure supplement 1C*). In some dead *Styxl2* KO fetuses, edema was found (*Figure 2B*), suggesting potential problems with the heart (*Conway et al., 2003*). This is consistent with the fact that Styxl2 is also highly expressed in cardiac muscles as well. The electron microscopy analysis of the heart muscles from E14.5 embryos revealed that the sarcomeric structures of cardiac muscles from *Styxl2* KO embryos were severely disrupted (*Figure 2C*). To focus on the functions of Styxl2 in skeletal muscles, we generated conditional *Styxl2* KO (CKO) mice by crossing *Styxl2^{f/f}* mice with *Pax7^{Cre/+}* mice (*Keller et al., 2004*; *Figure 2—figure supplement 1D*).

We found that *Styxl2* CKO pups were born at the expected Mendelian ratio but all the homozygous mutant pups died in a few hours after birth (*Figure 2D and E* and *Figure 2—figure supplement 1D*). As Pax7 is also expressed in other non-muscle cell types including neurons during embryo development, to be certain that embryonic lethality of *Pax7^Cre/+^; Styxl2^f/f^* mice was indeed caused by severe defects in skeletal muscles, we also specifically deleted *Styxl2* in skeletal muscles using a *Myf5^Cre^* line in which the *Cre* gene was inserted in the *Myf5* locus (*Tallquist et al., 2000*). Consistently, all skeletal muscle-specific *Styxl2* KO pups died within one day after birth (*Figure 2—figure supplement 1D*).

As the skin of *Styxl2* CKO pups appeared cyanotic, we speculated that the new-born mutant mice had lung defects that led to respiratory distress and perinatal death. The lungs of the CKO pups were examined and we found that the pulmonary alveoli indeed failed to open (*Figure 2F*), which was likely caused by defective diaphragm muscle as defects in a number of myogenic genes exhibited similar perinatal lethality (*Hasty et al., 1993*; *Rudnicki et al., 1993*). Electron microscopy analysis confirmed that the sarcomere structure was severely disrupted in diaphragm muscle of the mutant mice (*Figure 2G*). Consistently, electron microscopy revealed that the sarcomere structure of the limb muscle was also severely disrupted (*Figure 2—figure supplement 1E*). Notably, some sarcomeres were still present in the skeletal muscles of the CKO mice (*Figure 2—figure supplement 1E*), suggesting that Styxl2 is important but not absolutely required for the formation of the sarcomeres. Therefore, Styxl2 plays an important role in the development of striated muscles, including the skeletal muscle and the heart muscle.

Styxl2 is dispensable for the maintenance of mature sarcomeres but critical for de novo sarcomere assembly in adult skeletal muscles

Although our data above indicated that Styxl2 plays an important role in regulating sarcomere formation during embryonic skeletal muscle development, it remained unclear whether it was necessary for the maintenance of the sarcomere structure in adult skeletal muscles. To address this question, we generated a tamoxifen (TMX) inducible myofiber-specific *Styxl2* knockout mouse model (also named *Styxl2* MF-iKO hereafter) using Tg (HSA-MerCreMer) (*McCarthy et al., 2012*). In this model, *Styxl2* was efficiently deleted in mature skeletal muscles of adult mice (*Figure 3A and B*). We directly assessed the contractile functions of Styxl2-null muscles. Three weeks after the last TMX injection (*Figure 3A*), the gastrocnemius muscle was isolated and the twitch and tetanic force generated by the muscle were measured (*Guo et al., 2016*). No obvious difference in twitch or tetanic force was observed between the control and *Styxl2* MF-iKO muscles (*Figure 3C and D*), suggesting that Styxl2 is dispensable for the maintenance of existing sarcomeres in adult skeletal muscles. Next, we assessed whether Styxl2 played a role in the de novo formation of nascent sarcomeres in regenerating muscles of adult mice. To do so, we generated another tamoxifen-inducible, MuSC-specific *Styxl2* KO mouse model using *Pax7^CreERT2/CreERT2^; Styxl2^f/f^* (also named *Styxl2* SC-iKO mice hereafter) (*Murphy et al., 2011*). *Styxl2* was first deleted in muscle satellite cells (MuSCs) of adult mice according to the scheme in *Figure 3E*, followed by acute injury to the hindlimb skeletal muscles with Cardiotoxin (CTX) (*Figure 3E*). As injured muscles are repaired by MuSCs, the nascent sarcomeres in regenerating myofibers of *Styxl2* SC-iKO mice would be formed in the absence of Styxl2 (*Figure 3F*). At 30 days post-injury, a time point when injured muscles are known to be fully regenerated (*Dumont et al., 2015*), the gastrocnemius muscles were isolated and functionally tested in vitro. Both the twitch and tetanic force were measured separately. Compared to muscles from the control mice, the twitch force generated by muscles from *Styxl2* SC-iKO mice was decreased by ~30% (*Figure 3G*), while the tetanic force generated by muscles from the mutant mice was not affected (*Figure 3H*). This suggested that sarcomeres formed de novo in regenerating myofibers from Styxl2-null MuSCs were partially defective. When we examined sarcomeres by electron microscopy, we noticed that the length of individual sarcomeres from *Styxl2* SC-iKO mice was shorter in regenerated muscles (*Figure 3I and J*). Thus, our data showed that Styxl2 functions in de novo sarcomere assembly in regenerating muscles from adult mice.

Styxl2 directly binds to non-muscle myosin II (NM II) in myoblasts

To understand how Styxl2 functions to regulate sarcomere formation, we employed BioID, a proximity-dependent protein labelling method (*Roux et al., 2012*; *Roux et al., 2018*), to search for binding partners of Styxl2. The full-length Styxl2 was fused in-frame with BirA*, a mutant form of biotin ligase BirA (*Figure 4A*). The fused gene encoding Styxl2-BirA*-HA was stably expressed
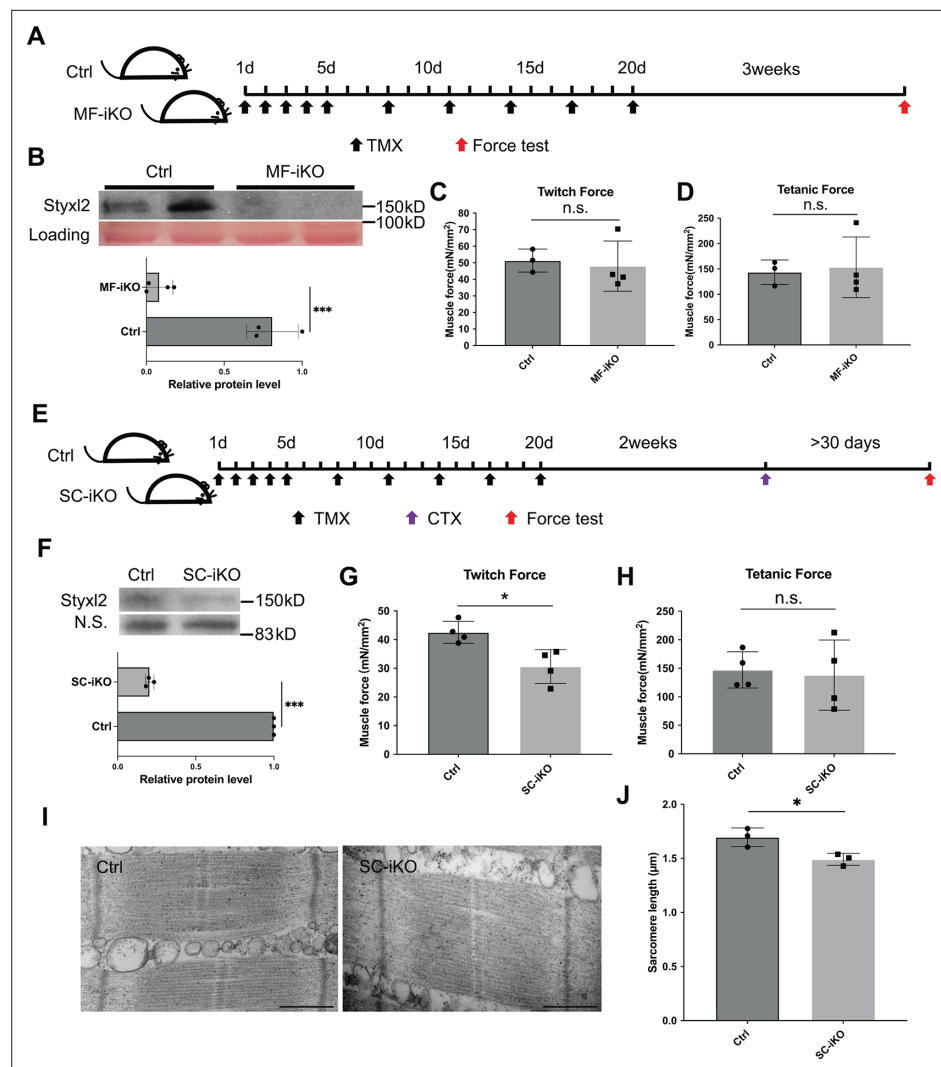
Figure 3. Styxl2 is not required for sarcomere maintenance but involved in de novo sarcomere assembly in adult muscles. (**A**) The schematic to assess the role of Styxl2 in sarcomere maintenance in adult muscles. TMX: tamoxifen. (**B**) Styxl2 protein levels in control (Ctrl) and myofiber-specific *Styxl2* knockout (MF-iKO) mouse gastrocnemius muscles used for force test. The band intensity of Styxl2 was quantified by ImageJ. (**C, D**) The twitch and tetanic force generated by gastrocnemius muscles of three Ctrl and four MF-iKO mice were measured. In (**A–D**), Ctrl: *Styxl2$^{f/f}$* mice; MF-iKO: *Tg: HSA-MerCreMer; Styxl2$^{f/f}$* mice. (**E**) The schematic to assess the role of Styxl2 in de novo sarcomere assembly in adult muscles. CTX: cardiotoxin. (**F**) Styxl2 protein levels in regenerated gastrocnemius muscles used for force test. N.S.: non-specific. The band intensity of Styxl2 was quantified. (**G, H**) Twitch and tetanic force by regenerated gastrocnemius muscles were measured from four pairs of control and MuSC-specific *Styxl2* KO (SC-iKO) mice. (**I**) Transmission electron microscopy (TEM) images of the muscle used for force generation test. Scale bar: 500 nm. (**J**) Quantification of sarcomere length in (**I**). TEM images from three pairs of mice were examined and the length of 3–5 sarcomeres from each mouse was measured. In (**E–J**), Ctrl: *Pax7$^{CreERT2/CreERT2}$* mice; SC-iKO: *Pax7$^{CreERT2/CreERT2}$; Styxl2$^{f/f}$* mice. n.s.: not significant. *p-value <0.05. ***p-value <0.001.

The online version of this article includes the following source data for figure 3:

Source data 1. Original scans for the Western blot analysis in *Figure 3B* (anti-Styxl2 and Loading).

Source data 2. A PDF file showing original scans of the relevant Western blot analysis in *Figure 3B* (anti-Styxl2 and Loading) with highlighted bands and sample labels.

Source data 3. Original scans for the Western blot analysis in *Figure 3F* (anti-Styxl2 and N.S.).

Source data 4. A PDF file showing original scans of the relevant Western blot analysis in *Figure 3F* (anti-Styxl2 and N.S.) with highlighted bands and sample labels.
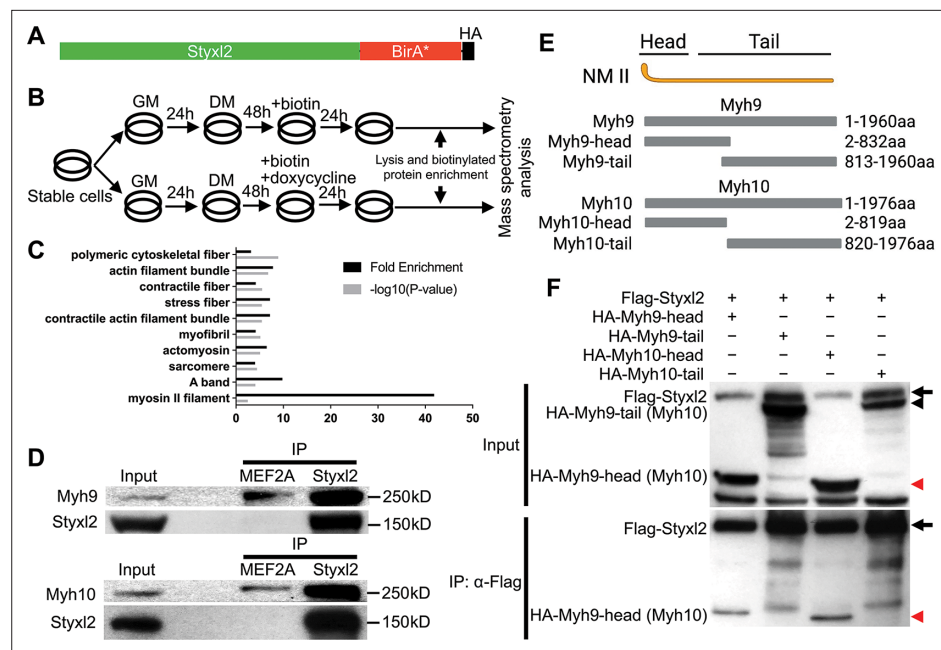
Figure 4. Styxl2 binds to non-muscle myosin IIs. (**A**) The schematic of the fusion protein Styxl2-BirA*-HA. (**B**) The workflow of sample preparation for BioID. (**C**) Enriched (with Enrichment score >1) biotinylated proteins in cells expressing Styxl2-BirA*-HA relative to that in control cells were identified by mass spectrometry followed by Gene Ontology (GO) analysis. Myofibril-related terms were shown. (**D**) C2C12 cells were harvested after 2 days in differentiation medium (DM) and the soluble whole cell lysates were subjected to immunoprecipitation (IP) using either an anti-MEF2A (negative control) or an anti-Styxl2 antibody. The endogenous Myh9 or Myh10 was detected by Western blot. (**E**) The schematic shows the domains of non-muscle myosin IIs (NM II). (**F**) HEK 293T cells were transfected with Flag-Styxl2 (black arrow) together with HA-NM II-head (red arrowheads) or HA-NM II-tail (black arrowheads). The soluble whole cell lysates were subjected to IP with an anti-Flag antibody and the co-immunoprecipitated proteins were detected by Western blot.

The online version of this article includes the following source data and figure supplement(s) for figure 4:

Source data 1. Original scans for the Western blot analysis of input and IP in *Figure 4D* (anti-Styxl2, anti-Myh9, and anti-Myh10).

Source data 2. A PDF file showing original scans of the relevant Western blot analysis in *Figure 4D* (anti-Styxl2, anti-Myh9, and anti-Myh10) with highlighted bands and sample labels.

Source data 3. Original scans for the Western blot analysis of input and IP in *Figure 4F* (anti-Flag and anti-HA).

Source data 4. A PDF file showing original scans of the relevant Western blot analysis in *Figure 4F* (anti-Flag and anti-HA) with highlighted bands and sample labels.

Figure supplement 1. Identification of Styxl2-interacting partners by BioID.

Figure supplement 1—source data 1. Original scans for the Western blot analysis in *Figure 4—figure supplement 1A* (Streptavidin-HRP, anti-Styxl2, and Loading).

Figure supplement 1—source data 2. A PDF file showing original scans of the relevant Western blot analysis in *Figure 4—figure supplement 1A* (Streptavidin-HRP, anti-Styxl2, and Loading) with highlighted bands and sample labels.

Figure supplement 1—source data 3. An Excel file showing raw data of iTRAQ-based mass spectrometry analysis for potential Styxl2 interactors in *Figure 4—figure supplement 1B*.

---

in C2C12 myoblasts using the Tet-on system (*Das et al., 2016*; *Figure 4—figure supplement 1A*). As Styxl2 is expected to function during late myogenic differentiation, we followed the scheme in *Figure 4B* and added biotin into the culture medium with or without doxycycline (Dox) for 24 hr before harvest. By Western blot, we showed that Styxl2-BirA*-HA was strongly induced by Dox as expected (*Figure 4—figure supplement 1A*, middle panel). Importantly, more cellular proteins were biotinylated in Styxl2-BirA*-HA-expressing cells induced by Dox (*Figure 4—figure supplement 1A*, top panel). These biotinylated proteins were isolated and enriched by streptavidin beads

and analysed by iTRAQ-based mass spectrometry (*Wiese et al., 2007*). The biotinylated proteins enriched in Styxl2-BirA*-HA-expressing cells (Enrichment score >1) were further analysed by gene ontology (GO) analysis. Notably, a number of the enriched proteins were related to 'myofibril', 'sarcomere', and 'A band' (*Figure 4C*). This supports our hypothesis that Styxl2 functions to regulate sarcomere assembly. To help identify direct interaction partners of Styxl2, the $\log_2$ Enrichment scores (i.e. the peak intensity ratios of the reporter ions) were plotted against the minus $\log_{10}$(p.values). Those enriched proteins with the Enrichment score >1.2 and p<0.05 were highlighted in red on the plot (*Figure 4—figure supplement 1B*), and some of the enriched proteins (*Figure 4—figure supplement 1C*) were selected for further confirmation by co-immunoprecipitation (co-IP) assays using lysates from differentiated C2C12 myotubes. Among them, Myh9 and Myh10, the members of the non-muscle myosin IIs (NM IIs) (*Newell-Litwa et al., 2015*), were found to specifically interact with the endogenous Styxl2 (*Figure 4D*). Moreover, by protein truncation analysis in combination with the co-IP assays, we showed that the head domains of Myh9 and Myh10 were responsible for their interaction with Styxl2 (*Figure 4E and F*).

Styxl2 promotes sarcomere assembly by down-regulating NM IIs

Our data above indicated that Styxl2 regulates sarcomere assembly. NM IIs were reported to participate in sarcomere assembly in several organisms (*Fenix et al., 2018*; *Sanger et al., 2009*; *Tullio et al., 1997*). However, NM IIs are not detected in mature sarcomeres and their replacement by muscle-specific myosin is a marker of skeletal muscle maturation. Therefore, we examined protein levels of Myh9 and Myh10 in both differentiating C2C12 myotubes and postnatal mouse skeletal muscles over time. In differentiating C2C12 cells, we found that the protein levels of Myh9 and Myh10 slightly increased at the beginning of myogenic differentiation, but started to decrease ~four days after myogenic differentiation, which coincided with the time when the sarcomeric myosin heavy chain started to increase (*Figure 5—figure supplement 1A*). In postnatal mouse skeletal muscles, the protein levels of Myh9 and Myh10 started to drop at P8 and became non-detectable by P30 (*Figure 5A*), which was consistent with previous reports (*Fenix et al., 2018*; *Sanger et al., 2009*). The protein levels of Styxl2 remained constant and abundant in the first month after birth but began to drop to a lower level by P65 (*Figure 5A*). When we examined the protein levels of Myh9 and Myh10 in skeletal muscles of P1 pups, we noticed an obvious increase in protein levels of Myh9 and Myh10 in *Styxl2* CKO mice (*Figure 5B and C*). We also examined protein levels of Myh9 and Myh10 in regenerating adult muscles. Using SC-iKO mice and *Pax7*$^{CreERT2/CreERT2}$ control mice as described in *Figure 3E*, we first induced *Styxl2* deletion by tamoxifen in adult MuSCs followed by BaCl$_2$-induced muscle injury. At 7 dpi, the levels of Myh9 and Myh10 were comparable between control and *Styxl2* SC-iKO mice (*Figure 5D*). Interestingly, at 10 dpi, Myh9 and Myh10 were nearly undetectable in muscles from control mice, but they remained at a higher level in muscles from *Styxl2* SC-iKO mice (*Figure 5D*). Our data above suggested that loss of Styxl2 results in delayed degradation of NM II during sarcomere assembly. To further prove this is the case, we turned to the zebrafish model. It was reported that *Styxl2*$^{-/-}$ zebrafish exhibited severe motility defects in response to needle touch (*Fero et al., 2014*). Consistently, we also found that *Styxl2* morphants displayed similar phenotypes: most of the *Styxl2* morphants did not respond to the needle touch (*Figure 5E*), which was caused by defective sarcomere structures in skeletal muscles (*Figure 5F*). Knowing that NM IIs are involved in the early phase of sarcomere assembly followed by their replacement with the sarcomeric myosin (*Fenix et al., 2018*; *White et al., 2014*), we suspected that delayed degradation of NM IIs was responsible for defective sarcomere structure in *Styxl2* morphants. Therefore, it was likely that simultaneous knockdown of both NM IIs and *Styxl2* may rescue the sarcomeric defects in *Styxl2* morphants. It was reported that both *Myh9b* and *Myh10* are expressed in skeletal muscles of zebrafish (*Gutzman et al., 2015*). When we knocked down *Myh9b* with a MO in *Styxl2* morphants, the embryos died very early before skeletal muscles were formed (our unpublished data). When zebrafish zygotes were co-injected with the *Styxl2*-MO and a MO targeting *Myh10* (*Figure 5—figure supplement 1B*), the percentage of fishes responding to the needle touch was obviously increased (*Figure 5E*). Consistently, the disrupted sarcomere structure caused by *Styxl2*-MO was indeed partially restored in the *Styxl2/Myh10* double-knockdown fishes (*Figure 5F*).
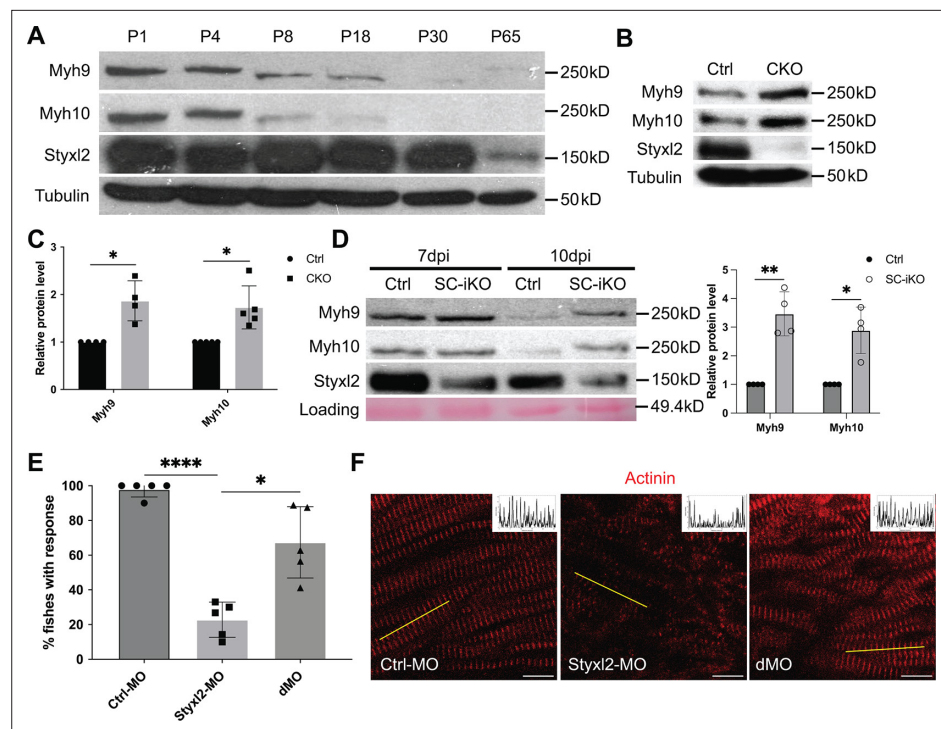
Figure 5. Styxl2 protein levels inversely correlates with that of non-muscle myosin IIs. (**A**) Protein levels of Styxl2 and non-muscle myosin IIs in skeletal muscles of wild-type mice of different ages were determined by Western blot. (**B**) Protein levels of Styxl2 and non-muscle myosin IIs in skeletal muscles of control and *Styxl2* conditional KO (CKO) P1 mice were determined by Western blot. (**C**) Relative ratios of non-muscle myosin II protein levels in control and *Styxl2* CKO P1 mice were quantified by ImageJ based on the data from four (for Myh9) or five (for Myh10) sets of Western blots. (**D**) Protein levels of Styxl2 and non-muscle myosin IIs in regenerating tibialis anterior muscles were determined by Western blot. The experiments were done for four times with similar results and a representative gel was shown. The protein levels of NM IIs in 10 dpi muscles revealed by Western blot were quantified in the right panel. Ctrl: *Pax7^{CreERT2/CreERT2}* mice; SC-iKO: *Pax7^{CreERT2/CreERT2}*; *Styxl2^{f/f}* mice; dpi: days post-injury. (**E**) Zebrafish zygotes were separately injected with the following morpholinos (MO): control (Ctrl-MO), *Styxl2*-MO, and mixed morpholinos targeting both *Styxl2* and *Myh10* (dMO). At 48 hpf, zebrafishes were poked by a fine needle and their responses were recorded. Quantification of responses of zebrafish to needle touch was shown. In each group, at least eight zebrafishes were tested and the percentage of zebrafishes responding to needle touch was calculated. Each dot represents one group of experiment. (**F**) Zebrafishes from each condition in (**E**) were subjected to immunostaining for α-actinin to visualize sarcomere structures. Representative images were shown. The inset at the top right corner of each image shows the actinin intensity along the yellow line. Scale bar: 10 μm. *p-value <0.05. **p-value <0.01. ****p-value <0.0001.

The online version of this article includes the following source data and figure supplement(s) for figure 5:

Source data 1. Original scans for the Western blot analysis in *Figure 5A* (anti-Styxl2, anti-Myh9, anti-Myh10 and anti-Tubulin).

Source data 2. A PDF file showing original scans of the relevant Western blot analysis in *Figure 5A* (anti-Styxl2, anti-Myh9, anti-Myh10, and anti-Tubulin) with highlighted bands and sample labels.

Source data 3. Original scans for the Western blot analysis in *Figure 5B* (anti-Styxl2, anti-Myh9, anti-Myh10, and anti-Tubulin).

Source data 4. A PDF file showing original scans of the relevant Western blot analysis in *Figure 5B* (anti-Styxl2, anti-Myh9, anti-Myh10, and anti-Tubulin) with highlighted bands and sample labels.

Source data 5. Original scans for the Western blot analysis in *Figure 5D* (anti-Styxl2, anti-Myh9, anti-Myh10, and Loading).

Source data 6. A PDF file showing original scans of the relevant Western blot analysis in *Figure 5D* (anti-Styxl2, anti-Myh9, anti-Myh10, and Loading) with highlighted bands and sample labels.

Figure supplement 1. The protein levels of NM IIs in differentiating C2C12 cells and the knockdown efficiency of Myh10-MO.

Figure 5 continued on next page

Figure supplement 1—source data 1. Original scans for the Western blot analysis in *Figure 5—figure supplement 1A* (anti-MHC, anti-Myh9, anti-Myh10, anti-Styxl2, and anti-Tubulin).

Figure supplement 1—source data 2. A PDF file showing original scans of the relevant Western blot analysis in *Figure 5—figure supplement 1A* (anti-MHC, anti-Myh9, anti-Myh10, anti-Styxl2, and anti-Tubulin) with highlighted bands and sample labels.

Figure supplement 1—source data 3. Original scans for the Western blot analysis in *Figure 5—figure supplement 1B* (anti-Myh10 and anti-Tubulin).

Figure supplement 1—source data 4. A PDF file showing original scans of the relevant Western blot analysis in *Figure 5—figure supplement 1B* (anti-Myh10 and anti-Tubulin) with highlighted bands and sample labels.

Styxl2 induces the degradation of NM IIs via its C-terminal domain

Our data above showed that loss of Styxl2 caused abnormal accumulation of NM IIs (*Figure 5*), which suggested that Styxl2 normally promote degradation of NM IIs during nascent sarcomere assembly. To test whether this is the case, we co-expressed HA-Myh9 with either Mst1 (as a negative control) or Styxl2 in C2C12 myoblasts. The protein levels of HA-Myh9 were indeed reduced by co-transfected
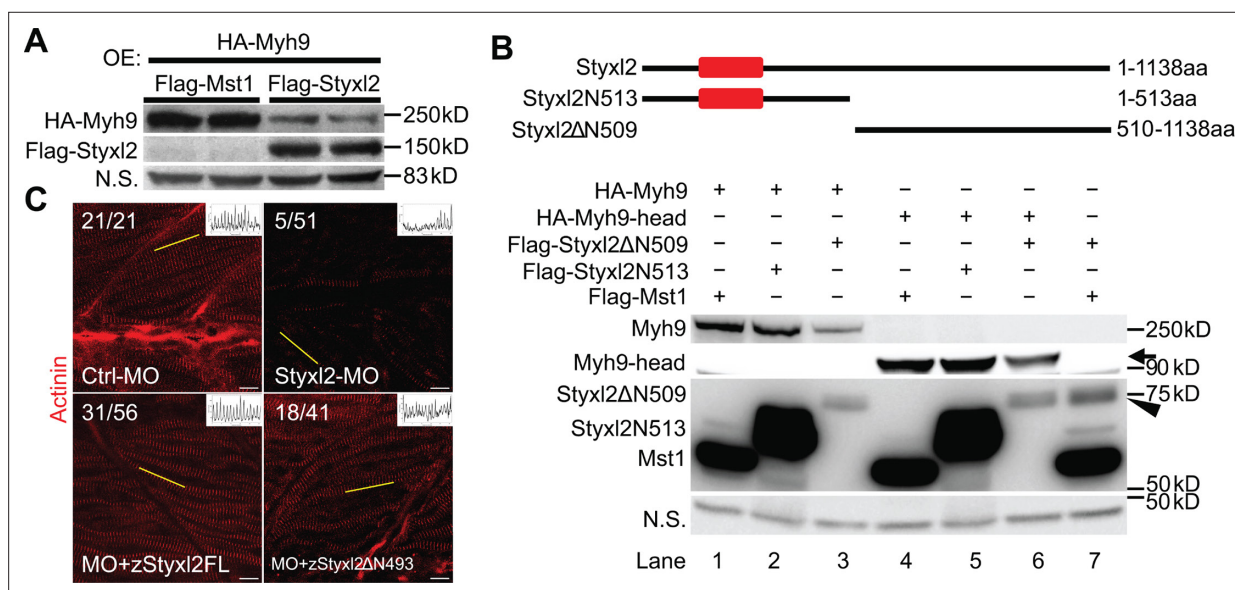

Figure 6. The dual-specificity phosphatase catalytic (DSPc) domain of Styxl2 is dispensable for degradation of non-muscle myosin IIs. (**A**) DNA constructs encoding Myh9, Styxl2, or Mst1 (negative control) were co-expressed in C2C12 cells. Soluble whole cell extracts were subjected to Western blot analysis. OE: overexpression. (**B**) The schematic shows the truncated fragments of Styxl2 protein. The red blocks indicate the DSPc domain of Styxl2. HEK 293T cells were transfected with different plasmids as indicated. 24 hr after transfection, cells were harvested, and soluble whole cell extracts were subjected to Western blot analysis. The arrow indicates the head domain of Myh9, and the arrowhead indicates Styxl2 missing the N-terminal 509 aa (Styxl2ΔN509). Mst1: negative control. N.S.: non-specific. (**C**) Zebrafish zygotes were injected with various morpholinos as indicated with or without the co-injected *Styxl2* mRNAs. z*Styxl2*FL: the full-length fish *Styxl2* mRNA; z*Styxl2*ΔN493: the truncated fish *Styxl2* mRNA missing the 5' region encoding the N-terminal 493 aa. Representative α-actinin immunofluorescent images were shown. The number in numerator at the top left corner of each image represents fish embryos showing normal α-actinin staining pattern, while that in denominator represents the total number of embryos examined. The inset at the top right corner of each image shows the actinin intensity along the yellow line. Scale bar: 10 μm.

The online version of this article includes the following source data and figure supplement(s) for figure 6:

Source data 1. Original scans for the Western blot analysis in *Figure 6A* (anti-Flag, anti-HA, and N.S.).

Source data 2. A PDF file showing original scans of the relevant Western blot analysis in *Figure 6A* (anti-Flag, anti-HA, and N.S.) with highlighted bands and sample labels.

Source data 3. Original scans for the Western blot analysis in *Figure 6B* (anti-Flag, anti-HA, and N.S.).

Source data 4. A PDF file showing original scans of the relevant Western blot analysis in *Figure 6B* (anti-Flag, anti-HA, and N.S.) with highlighted bands and sample labels.

Figure supplement 1. Styxl2 regulates the protein levels of NM IIs without affecting their mRNA.

Styxl2 (*Figure 6A*). We further found that Styxl2-mediated reduction in Myh9 protein levels was not caused by reduced *Myh9* mRNA (*Figure 6—figure supplement 1A*). To determine which part of Styxl2 promotes degradation of NM IIs, we truncated Styxl2 into two fragments (*Figure 6B*, upper panel): an N-terminal fragment containing the DSPc domain (i.e. aa 1–513, also termed Styxl2N513 hereafter) and a C-terminal fragment without the DSPc domain (i.e. aa 510–1138, also named Styxl2ΔN509 hereafter). When we co-transfected 293T cells with a construct encoding HA-Myh9 together with another construct encoding Mst1, Styxl2N513, or Styxl2ΔN509, we found that only Styxl2ΔN509 promoted degradation of Myh9 (*Figure 6B*, lane 3). As we previously showed that the head domains of NM IIs were involved in interacting with Styxl2 (*Figure 4E and F*), we then tested whether the protein levels of the head domain of Myh9 were also regulated by Styxl2. Consistently, only Styxl2ΔN509 promoted degradation of the head domain of Myh9 (*Figure 6B*, lane 6). To further verify this finding in vivo, we microinjected the mRNA encoding the full-length or the C-terminus of zebrafish Styxl2 (zStyxl2), along with the MO for z*Styxl2*, into the zebrafish one-cell embryos. As expected, the defective sarcomere structure caused by *zStyxl2* knockdown was efficiently rescued by overexpressing the mRNA encoding the full-length zStyxl2, as revealed by the α-actinin staining (*Figure 6C*). Importantly, the mRNA encoding the C-terminus of zStyxl2 was nearly as effective as that encoding the full-length zStyxl2 (*Figure 6C*). Similar results were also obtained when we subjected fish to myosin staining (*Figure 6—figure supplement 1B*). Thus, the C-terminus of Styxl2, without the DSPc domain, is both necessary and sufficient to promote degradation of NM IIs during nascent sarcomere assembly.

Styxl2 promotes the degradation of NM IIs via the autophagy-lysosome pathway

In order to understand how Styxl2 promotes the degradation of NM IIs, we first turned to the ubiquitination/proteasome pathway (*Nandi et al., 2006*). MG132, a specific proteasome inhibitor, was added to C2C12 cells transfected with Styxl2. No abnormal accumulation of NM IIs was found in the presence of MG132 (*Figure 7—figure supplement 1*), suggesting that the proteasome is not involved in Styxl2-mediated degradation of NM IIs. Next, we turned to the autophagy-lysosome-dependent protein degradation system. In C2C12 myoblasts, we co-expressed Myh9 with either Mst1 (control) or Styxl2 together with an siRNA against GFP (control) or ATG5, a key component of the autophagy pathway (*Mizushima et al., 2010*). In the presence of the control siRNA, Styxl2 efficiently promoted degradation of Myh9 as expected (*Figure 7A*, lane 2). However, in the presence of ATG5 siRNA, the protein levels of Myh9 were restored to levels comparable to that of the control even in the presence of the co-expressed Styxl2 (*Figure 7A*, lane 3). This result supported the involvement of the autophagy pathway in Styxl2-mediated degradation of NM IIs. Furthermore, we also examined the degradation of Myh9 induced by Styxl2Δ509 with or without several different autophagy inhibitors (*Figure 7B*). In the absence of any autophagy inhibitors, Styxl2ΔN509 induced degradation of Myh9 as expected (*Figure 7B*, lanes 3 and 4). In the presence of LY294002 (an inhibitor of PI3K), chloroquine (an inhibitor that blocks the binding of autophagosomes to lysosomes), bafilomycin A1 (BafA1, an inhibitor of V-ATPase that can block autophagic flux), and NH_4Cl (an inhibitor of the degradative enzymes inside lysosomes), the protein levels of Myh9 were largely restored to the levels comparable to that in the controls (*Figure 7B*, lanes 1 and 2). Thus, we concluded that the autophagy-lysosome pathway is involved in the degradation of NMIIs induced by Styxl2.

It is known that some ubiquitinated proteins (such as sarcomeric titin) are degraded by selective autophagy (*Bogomolovas et al., 2021*; *Chen et al., 2019*; *Kirkin et al., 2009*; *Pankiv et al., 2007*; *Shaid et al., 2013*; *Zaffagnini and Martens, 2016*). A recent report showed that Myh9 could also undergo Nek9-mediated selective autophagy (*Yamamoto et al., 2021*), suggesting that Myh9 is ubiquitinated. To find out whether Styxl2 promotes ubiquitination of NM IIs, we co-transfected HEK 293T cells with plasmids encoding Myh9 and ubiquitin together with a plasmid encoding either Mst1 or Styxl2. Compared to the Mst1 control, we found that Styxl2 indeed promoted the ubiquitination of Myh9 (*Figure 7C*).
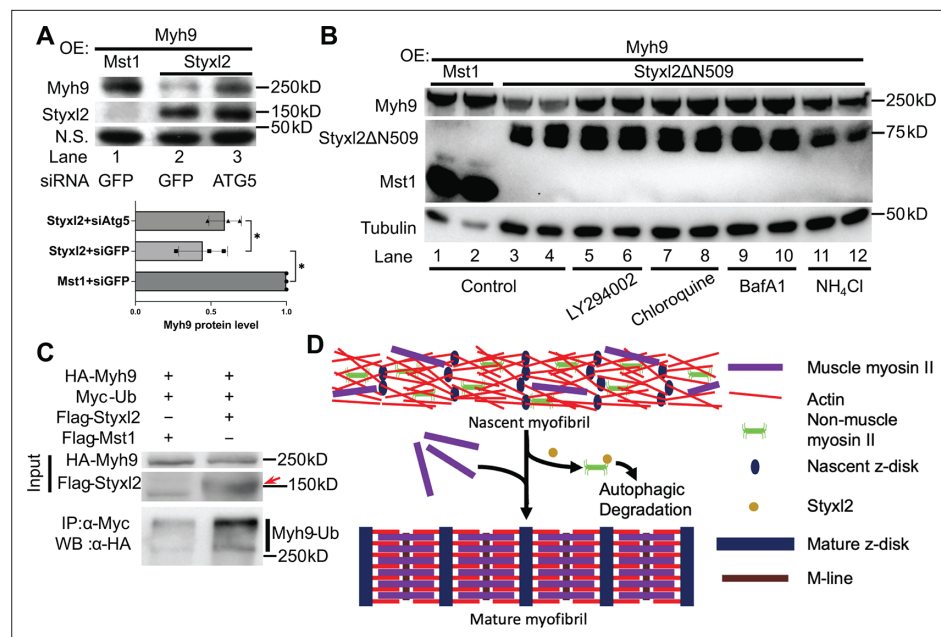
Figure 7. The Styxl2-mediated degradation of non-muscle myosin IIs is autophagy dependent. (**A**) Plasmids encoding Myh9, Styxl2, or Mst1 (negative control) were co-expressed in C2C12 cells together with various siRNAs as indicated. Soluble whole cell extracts were subjected to Western blot analysis. OE: overexpression. N.S.: non-specific. The protein level of Myh9 was quantified at the bottom panel. *p-value <0.05. (**B**) HEK 293T cells were transfected with various constructs as indicated. Various inhibitors of the autophagy-lysosome pathway (50 μM LY294002, 100 μM Chloroquine, 100 nM BafA1, 20 mM NH₄Cl) were added to the cell culture 6 hr before harvest. OE: overexpression. (**C**) HEK 293T cells were co-transfected with the plasmids as indicated. 18 hr later, 100 nM of BafA1 was added to the culture medium. After another 6 hr, the soluble whole cell lysates were subjected to immunoprecipitation (IP) with an anti-Myc antibody, and the immunoprecipitated proteins were further analysed by Western blot (WB). The red arrow indicates Flag-Styxl2. (**D**) The schematic shows that Styxl2 promotes sarcomere assembly by binding to and targeting non-muscle myosin IIs for degradation, which facilitates their eventual replacement by muscle myosin II during sarcomere maturation.

The online version of this article includes the following source data and figure supplement(s) for figure 7:

Source data 1. Original scans for the Western blot analysis in *Figure 7A* (anti-Styxl2, anti-Myh9, and N.S.).

Source data 2. A PDF file showing original scans of the relevant Western blot analysis in *Figure 7A* (anti-Styxl2, anti-Myh9, and N.S.) with highlighted bands and sample labels.

Source data 3. Original scans for the Western blot analysis in *Figure 7B* (anti-Myh9, anti-Styxl2ΔN509, anti-Mst1, and anti-Tubulin).

Source data 4. A PDF file showing original scans of the relevant Western blot analysis in *Figure 7B* (anti-Myh9, anti-Styxl2ΔN509, anti-Mst1, and anti-Tubulin) with highlighted bands and sample labels.

Source data 5. Original scans for the Western blot analysis of input and IP in *Figure 7C* (anti-Flag and anti-HA).

Source data 6. A PDF file showing original scans of the relevant Western blot analysis in *Figure 7C* (anti-Flag and anti-HA) with highlighted bands and sample labels.

Figure supplement 1. Proteasome is not involved in Styxl2-mediated degradation of NM IIs.

Figure supplement 1—source data 1. Original scans for the Western blot analysis in *Figure 7—figure supplement 1* (anti-Myh9, anti-Myh10, anti-Styxl2, and Loading).

Figure supplement 1—source data 2. A PDF file showing original scans of the relevant Western blot analysis in *Figure 7—figure supplement 1* (anti-Myh9, anti-Myh10, anti-Styxl2, and Loading) with highlighted bands and sample labels.

Discussion

Styxl2 is a pseudophosphatase that functions independently of its conserved phosphatase domain

Pseudophosphatases are present in multicellular organisms ranging from *C. elegans* to humans

(*Hinton, 2019*; *Reiterer et al., 2020*). Moreover, pseudophosphatases have also been identified in plants (*Bellec et al., 2002*). Recently, 26 pseudophosphatase domains, including the phosphatase domain of Styxl2, were bioinformatically identified in the human genome (*Chen et al., 2017*). Due to the absence of one or several conserved amino acids including the catalytic cysteine, pseudo-phosphatases are not expected to possess the phosphatase activity. STYX, the first molecularly characterized pseudophosphatase, was identified in 1995 as a phosphoserine/threonine/tyrosine-binding protein (*Wishart et al., 1995*). The substitution of the catalytic cysteine by glycine in the active site motif leads to the loss of its catalytic activity (*Reiterer et al., 2013*; *Wishart et al., 1995*). In addition to STYX, the functions of several other pseudophosphatases from *C. elegans* to humans have also been characterized (*Cheng et al., 2009*; *Hinton et al., 2010*; *Maruyama et al., 2007*; *Nakhro et al., 2013*; *Tomar et al., 2019*). These reports unequivocally demonstrate that pseudophosphatases are not simply evolution relics but play essential roles in multicellular organisms.

Pseudophosphatases exert their functions via diverse modes including direct competition with other proteins by binding to a phospho-residue-containing motif, modulation of the phosphatase activity by binding to an active phosphatase, sequestration of target proteins in specific subcel-lular locations, and integration of signals by simultaneous binding with multiple proteins (*Hinton, 2019*; *Reiterer et al., 2020*). The original report on STYX showed that mutation of the glycine in the conserved HGX$_5$R motif back to cysteine restored the phosphatase activity (*Wishart et al., 1995*), suggesting that the three-dimensional structure of the phosphatase domain in STYX is still folded properly. Thus, some pseudophosphatases are thought to function by binding to specific phosphor-ylated substrates, which is the case for pseudophosphatases EGG-4/5 and Pas2 (*Bellec et al., 2002*; *Cheng et al., 2009*; *Da Costa et al., 2006*). In these examples, pseudophosphatases bind the phos-phorylated sites of selected target proteins through their inactive phosphatase domains and prevent them from binding other interacting proteins or active phosphatases. However, this is not the only way pseudophosphatases function. MTMR13, a pseudophosphatase, functions by binding to MTMR2, an active lipid phosphatase, to regulate its phosphatase activity. Mutations in either *MTMR13* or *MTMR2* are causally linked to human Type 4B Charcot-Marie-Tooth disease, an inherited disorder of the peripheral nervous system with abnormal nerve myelination (*Berger et al., 2006*; *Robinson and Dixon, 2005*).

Unlike several other characterized pseudophosphatases that function via their conserved phospha-tase domains, Styxl2 appears to function independently of its phosphatase domain as the phospha-tase domain of Styxl2 is dispensable for its ability to induce degradation of NM IIs and to rescue the sarcomere defects in the *Styxl2* morphant zebrafish (*Figure 6B and C*). Such a phosphatase domain-independent mode of action is also observed in His Domain Protein Tyrosine Phosphatase (HD-PTP or PTPN23), a pseudophosphatase known to facilitate endosomal cargo sorting and the degradation of multiple membrane receptors including epidermal growth factor receptor, platelet-derived growth factor receptor, MHC class I and Integrin α5β1 (*Doyotte et al., 2008*; *Kharitidi et al., 2015*; *Ma et al., 2015*; *Parkinson et al., 2015*). Interestingly, a truncated fragment of HD-PTP without its phosphatase domain is still capable of promoting endosomal trafficking of cargo proteins like epidermal growth factor (EGF) (*Doyotte et al., 2008*).

Styxl2 facilitates de novo sarcomere assembly by promoting autophagy-dependent degradation of non-muscle myosin IIs

Although absent in invertebrates, Styxl2 is expressed and conserved in vertebrates. The specific involvement of Styxl2 in sarcomere assembly is supported by its restricted expression in striated muscles. Interestingly, mutation in the coding region of *STYXL2* and abnormal CpG methylation at the *STYXL2* locus were detected in some patients with congenital heart defects (CHD), suggesting a possible link of *STYXL2* to CHD (*Arrington et al., 2012*; *Radhakrishna et al., 2016*). Moreover, its role in sarcomere assembly is also conserved in vertebrates as interference of the gene expression in zebrafish by either a transposon integration or morpholino oligos leads to severe defects in sarco-mere assembly (*Fero et al., 2014*; *Figure 1D and E*). However, Styxl2 is not essential for sarcomere assembly as sarcomeres in *Drosophila* flight muscles can normally assemble in the absence of a Styxl2 homolog. Furthermore, we could still find residual sarcomeres in skeletal muscles of conditional *Styxl2* KO mice (driven by either *Pax7^Cre* or *Myf5^Cre*) (*Figure 2—figure supplement 1E*).

Although the highly-ordered sarcomere structure has been known for many years, it remains controversial how sarcomeres correctly assemble. Several different but not mutually exclusive models have been proposed (*Rui et al., 2010*; *Sanger et al., 2006*; *Sanger et al., 2017*). Studies in *Drosophila*, *C. elegans*, and mice underscore an essential role for integrin in initiating the assembly of sarcomeres (*Rui et al., 2010*; *Sparrow and Schöck, 2009*). For example, β1 integrin was shown to be essential for sarcomere assembly in mice (*Schwander et al., 2003*). Among the existing sarcomere assembly models, the prevailing model of sarcomere assembly is called premyofibril model (*Rhee et al., 1994*; *Sanger et al., 2006*; *Sanger et al., 2017*). In this model, α-actinin, skeletal muscle actin, and non-muscle myosin IIs (NM IIs) first assemble to form mini-sarcomeres or premyofibrils at the cell periphery. Then, additional sarcomeric proteins like titin, nebulin, troponin, and myomesin will be incorporated and NM IIs will be eventually replaced by skeletal muscle myosin in mature sarcomeres (*White et al., 2014*; *White et al., 2018*). Consistent with this model, germline knockout of NM IIB (i.e. Myh10) in mice led to early lethality between E14.5 and birth and sarcomere structural defects in embryonic cardiomyocytes (*Tullio et al., 1997*). Similarly, defective sarcomeres were also observed in embryonic muscles of stage-17 mutant fly null for *zipper* (*zip*), the *Drosophila* gene encoding the heavy chain of NM II (*Bloor and Kiehart, 2001*; *Loison et al., 2018*). Moreover, a recent paper using human iPSC-derived cardiomyocytes demonstrated that nascent sarcomeres assemble directly from muscle actin stress fibers (*Fenix et al., 2018*). Both MYH9 and MYH10 are present in muscle actin stress fibers with MYH10 being essential for sarcomere assembly. Consistent with the premyofibril model, NM IIs are found to be replaced by muscle myosin IIs in mature sarcomeres (*Fenix et al., 2018*). Nevertheless, the view of the involvement of NM IIs in early sarcomere assembly is also challenged by several studies. Unlike germline knockout of NM IIB, cardiac-specific knockout of NM IIB in adult mice did not generate obvious defects in sarcomere structures (*Ma et al., 2009*). Although NM IIA is not detected in embryonic hearts, loss of cardiac NM IIB led to increased expression of NM IIA, suggesting that NM IIA may compensate for the loss of NM IIB in NM IIB-null embryonic cardiomyocytes (*Fenix et al., 2018*; *Tullio et al., 1997*). Moreover, it was also suspected that the cardiomyocyte-specific deletion of NM IIB occurs after the initial sarcomere assembly due to the expression timing of the Cre recombinase under the control of the cardiac α-MHC promoter (*Fenix et al., 2018*; *Ma et al., 2009*). Furthermore, a recent study using CRISPR/Cas9 to knock out *MYH9* and *MYH10* genes either individually or in combination in human iPSC-derived cardiomyocytes showed that neither gene is required for sarcomere assembly in their cell culture models (*Chopra et al., 2018*). It is puzzling at present why the results on the involvement of NM IIs in de novo sarcomere assembly differ in the two studies by Fenix et al. and Chopra et al. even though both studies used human iPSC-derived cardiomyocytes to assay de novo sarcomere assembly in cell culture.

It also remains unclear how NM IIs are replaced by muscle myosin during de novo sarcomere assembly in vertebrates. Our current study showed that Styxl2 interacts with NM IIs and induces their degradation via the autophagy-lysosome pathway. Autophagy is known to regulate sarcomere integrity (*Masiero et al., 2009*; *Nakai et al., 2007*). In particular, selective autophagy is known to degrade multiple ubiquitinated sarcomeric proteins including titin and filamin (*Arndt et al., 2010*; *Bogomolovas et al., 2021*). p62/SQSTM1 and NBR1 have been shown to act as adaptors linking ubiquitinated substrates to Atg8/LC3 that is localized on the membrane of autophagosome (*Kirkin et al., 2009*; *Pankiv et al., 2007*). Interestingly, a recent study on ciliogenesis showed that MYH9 is also degraded by selective autophagy in an NEK9-mediated manner (*Yamamoto et al., 2021*). Consistently, we found that Styxl2 promotes the ubiquitination of Myh9 (*Figure 7C*). It remains to be established whether Nek9 is involved in Styxl2-mediated autophagic degradation of NM IIs and whether ubiquitination of NM IIs is dependent on Nek9-mediated phosphorylation during myofibrillogenesis.

Our data showed that Styxl2 plays an indispensable role during embryonic myogenesis as conditional deletion of *Styxl2* during mouse embryo development using either *Pax7^Cre^* or *Myf5^Cre^* resulted in severe disruption of sarcomere structures in skeletal muscles and perinatal lethality (*Figure 2* and *Figure 2—figure supplement 1*). In contrast, inducible deletion of *Styxl2* in adult muscles only led to mild defects in sarcomere structures (*Figure 3F–J*). It is likely that additional unknown molecules can compensate for the loss of Styxl2 in adult regenerating muscles. Such distinct roles of Styxl2 during development are also supported by differential expression patterns of Styxl2 and NM IIs: both are abundantly expressed in new-born and juvenile mice. While the protein levels of Myh9 and Myh10 start to drop one week after birth and become undetectable by three weeks after birth, that of Styxl2

is relatively stable in the first month after birth but starts to drop sharply by two months after birth (*Figure 5A*). This is also consistent with our findings that Styxl2 is not required for the maintenance of the sarcomeres in adult muscles (*Figure 3A–D*).

In summary, our current study shows that Styxl2 critically regulates de novo sarcomere assembly by binding to NM IIs, enhancing their ubiquitination, and promoting their autophagic degradation, which ultimately facilitates sarcomere maturation in vivo (*Figure 7D*).

Materials and methods

Key resources table

Reagent type (species) or resource	Designation	Source or reference	Identifiers	Additional information
Gene (*M. musculus*)	Styxl2	GenBank	MGI:MGI:2685055	
Gene (*D. rerio*)	zStyxl2 (dusp27)	GenBank	ZFIN:ZDB-GENE-140513–1	
Genetic reagent (*M. musculus*)	Styxl2flox/flox	This paper		See Materials and methods, Section 1.
Genetic reagent (*M. musculus*)	EIIA-Cre	The Jackson Laboratory	Strain #:003724	
Genetic reagent (*M. musculus*)	Pax7CreERT2/+	The Jackson Laboratory	Strain #:017763	
Genetic reagent (*M. musculus*)	Myf5Cre/+	*Tallquist et al., 2000*		
Genetic reagent (*M. musculus*)	Pax7Cre/+	*Keller et al., 2004*		
Genetic reagent (*M. musculus*)	Tg (HSA-MerCreMer)	*McCarthy et al., 2012*		
Strain, strain background (*D. rerio*)	ABSR wild type fish	Prof. Zilong Wen (HKUST)		
Cell line (*M. musculus*)	C2C12	ATCC	CRL-1772	
Cell line (*Homo-sapiens*)	HEK 293T	ATCC	CRL-3216	
Transfected construct (*M. musculus*)	Flag-Styxl2	This paper		See Materials and methods, Section 2.
Transfected construct (*M. musculus*)	Flag-Styxl2ΔN509	This paper		See Materials and methods, Section 2.
Transfected construct (*M. musculus*)	Flag-Styxl2N513	This paper		See Materials and methods, Section 2.
Transfected construct (*M. musculus*)	Myosin-IIA-GFP	addgenen	#38297	
Transfected construct (*M. musculus*)	HA-Myh9	This paper		See Materials and methods, Section 2.
Transfected construct (*M. musculus*)	HA-Myh9-head	This paper		See Materials and methods, Section 2.
Transfected construct (*M. musculus*)	HA-Myh9-tail	This paper		See Materials and methods, Section 2.
Transfected construct (*M. musculus*)	HA-Myh10-head	This paper		See Materials and methods, Section 2.
Transfected construct (*M. musculus*)	HA-Myh10-tail	This paper		See Materials and methods, Section 2.
Transfected construct (*E. coli*)	pcDNA3.1 mycBioID	addgene	#35700	Re-cloned into pcDNA3.0.
Transfected construct (*D. rerio*)	zStyxl2	This paper		See Materials and methods, Section 2.
Transfected construct (*D. rerio*)	zStyxl2ΔN493	This paper		See Materials and methods, Section 2.
Antibody	anti-Jak1 (Rabbit Polyclonal)	Upstate	Cat#: 06–272	IB(1:2000)

Continued on next page

Continued

Reagent type (species) or resource	Designation	Source or reference	Identifiers	Additional information
Antibody	anti-Stat1 (Rabbit Polyclonal)	Upstate	Cat#: 06–501	IB(1:2000)
Antibody	anti-β-Tubulin (Mouse monoclonal)	Sigma	Cat#: T4026	IB(1:5000)
Antibody	anti-sarcomere MHC (Mouse monoclonal)	DSHB	MF20	IB(1:1000) IF(1:200)
Antibody	anti-GAPDH (Mouse Monoclonal)	Ambion	Cat#: AM4300	IB(1:10000)
Antibody	anti-Myh9 (Rabbit Polyclonal)	Cell Signaling	Cat#: 3403	IB(1:2000) IF(1:200)
Antibody	anti-Myh10 (Mouse monoclonal)	Santa Cruz	Cat#: sc-376942	IB(1:1000)
Antibody	anti-Flag (Mouse monoclonal)	Sigma	F3165	IF(1:5000)
Antibody	anti-HA (Mouse monoclonal)	Roche	12CA5	IB(1:5000)
Antibody	anti-Styxl2 (Rabbit Polyclonal)	This paper		See Materials and methods, Section 7. IB(1:500)
Antibody	anti-MEF2A (Rabbit Polyclonal)	This paper		Immunize rabbits with mouse MEF2A.
Antibody	anti-Flag (Rabbit Polyclonal)	Sigma	F7425	IF(1:200)
Antibody	anti-HA (Rabbit polyclonal)	Santa Cruz	Cat#: sc-805	IF(1:200)
Antibody	anti-Myc (Mouse monoclonal)	Santa Cruz	Cat#: sc-40	IB(1:1000)
Antibody	anti-α-Actinin (Mouse monoclonal)	Sigma	Cat#: A7732	IF(1:200)
Antibody	anti-Prox1 (Rabbit polyclonal)	Angiobio	Cat#: 11–002 P	IF(1:200)
Antibody	anti-slow myosin heavy chain (Mouse monoclonal)	DSHB	F59	IF(1:200)
Antibody	anti-myosin heavy chain (Mouse monoclonal)	DSHB	A4.1025	IF(1:200)
Recombinant DNA reagent	pRetroX-Tet-On Advanced (plasmid)	Dr. Yusong Guo (HKUST)		
Sequence-based reagent	Styxl2-F	This paper	PCR primers	GCCCATCCACCTCTCCTC
Sequence-based reagent	Styxl2-R	This paper	PCR primers	GCTCCTGTCATCCATCTTCTC
Sequence-based reagent	Myh9-F	This paper	PCR primers	GGCCCTGCTAGATGAGGAGT
Sequence-based reagent	Myh9-R	This paper	PCR primers	CTTGGGCTTCTGGAACTTGG
Sequence-based reagent	Myh10-F	This paper	PCR primers	GGAATCCTTTGGAAATGCGAAGA
Sequence-based reagent	Myh10-R	This paper	PCR primers	GCCCCAACAATATAGCCAGTTAC
Sequence-based reagent	Gapdh-F	This paper	PCR primers	CCCACTCTTCCACCTTCG
Sequence-based reagent	Gapdh-R	This paper	PCR primers	TCCTTGGAGGCCATGTAG
Sequence-based reagent	siGFP (negative control)	This paper	siRNA	GCTGACCCTGAAGTTCATC
Sequence-based reagent	siJak1	This paper	siRNA	GCCTGAGAGTGGAGGTAAC
Sequence-based reagent	siStat1	This paper	siRNA	GGATCAAGTCATGTGCATA
Sequence-based reagent	siATG5	This paper	siRNA	GGCTCCTGGATTATGTCAT
Sequence-based reagent	Ctrl (negative control)	This paper	morpholino	AGCACACAAAGGCGAAGGTCAACAT
Sequence-based reagent	Styxl2	This paper	morpholino	GCTGATCCTCCACAGACGACGCCAT
Sequence-based reagent	Myh10	This paper	morpholino	CTTCACAAATGTGGTCTTACCTTGA
Sequence-based reagent	Atg5	This paper	morpholino	CACATCCTTGTCATCTGCCATTATC
Chemical compound, drug	Cardiotoxin	Sigma Aldrich	Cat#: 217503	
Software, algorithm	ImageJ	National Institutes of Health		

Animals

ABSR wild-type zebrafish were maintained following standard procedures and the zygotes were collected for microinjection experiments. Pax7^{CreERT2/+} mice (Stock No: 017763) were purchased from the Jackson Laboratory (Bar Harbor, ME, USA). Myf5^{Cre/+}, Pax7^{Cre/+}, and Tg (HSA-MerCreMer) mice were generous gifts from Drs. Michael Rudnicki (Ottawa Hospital Research Institute, ON, Canada), Mario Capecchi (University of Utah, UT, USA), and Karyn Esser (University of Florida, FL, USA), respectively. Styxl2^{flox/flox} mice were generated by the Model Animal Research Centre (Nanjing University, Nanjing, China). To delete Styxl2 in adult mice, tamoxifen dissolved in corn oil (15 mg/ml) was injected into adult mice intraperitoneally at 5 µl per gram of body weight for five consecutive days followed by another five doses of tamoxifen injection every 3–4 days. All animals were maintained and handled following the protocols approved by the Animal Ethics Committee of the Hong Kong University of Science and Technology.

Cell culture and DNA constructs

C2C12 cells and HEK 293T cells were purchased from ATCC (Manassas, VA, USA). To ensure the cell quality, low-passage cells were used and the cell morphology was regularly examined. For C2C12 cells, the differentiation potential was also regularly examined by the expression of selected differentiation markers. In addition, DAPI staining was employed to detect the mycoplasma contamination in cell culture. C2C12 cells were maintained in growth medium (GM) (Dulbecco's modified Eagle's medium supplemented with 20% fetal bovine serum, 100 Units/ml penicillin, and 100 µg/ml streptomycin) and differentiation was induced with differentiation medium (DM) (Dulbecco's modified Eagle's medium supplemented with 2% horse serum, 100 Units/ml penicillin, and 100 µg/ml streptomycin). HEK 293T cells were maintained in Dulbecco's modified Eagle's medium supplemented with 10% fetal bovine serum, 100 Units/ml penicillin, and 100 µg/ml streptomycin. Mouse Styxl2, Styxl2ΔN509, and Styxl2N513 were amplified from a mouse muscle cDNA library and inserted into a modified pcDNA3.0 vector containing a Flag-expressing cassette to generate constructs encoding Flag-Styxl2, Flag-Styxl2ΔN509, and Flag-Styxl2N513. BirA* was amplified from pcDNA3.1 mycBioID (addgene, #35700) and an HA tag was added to its C-terminus. The cDNA encoding BirA*-HA was fused in-frame with that encoding mouse Styxl2 and cloned into the pRetroX-Tight-Pur vector (kindly provided by Dr. Yusong Guo at HKUST) to get pTight-Styxl2-BirA*-HA. Mouse Myh9, Myh9-head, and Myh9-tail were amplified from a plasmid encoding Myosin-IIA-GFP (addgene, #38297) and inserted into a modified pcDNA3.0 vector containing an HA-expressing cassette to generate constructs encoding HA-Myh9, HA-Myh9-head, and HA-Myh9-tail. Mouse Myh10-head and Myh10-tail were amplified from a mouse C2C12 cell cDNA library and inserted into a modified pcDNA3.0 vector containing an HA-expressing cassette to generate constructs encoding HA-Myh10-head and HA-Myh10-tail. Fish Styxl2 and Styxl2ΔN493 were amplified from a zebrafish cDNA library and inserted into pCS2+ vector to generate pCS2+-zStyxl2 and pCS2+-zStyxl2ΔN493.

RNA extraction and RT-qPCR

Total RNA was extracted from C2C12 cells using the TRIzol Reagent (Invitrogen) following the manufacturer's instructions. The reverse transcription was performed using an oligo-dT primer and the ImRrom-II Reverse Transcription System (Promega). The ABI 7700 Sequence Detection System (PE Applied-Biosystems) was used for qPCR and the relative fold change of genes of interest was analysed based on the $2^{-\Delta\Delta Ct}$ method (*Livak and Schmittgen, 2001*). The qPCR primers used were listed below:

Styxl2-F: 5'- GCCCATCCACCTCTCCTC-3'
Styxl2-R: 5'-GCTCCTGTCATCCATCTTCTC-3'
Myh9-F: 5'-GGCCCTGCTAGATGAGGAGT-3'
Myh9-R: 5'-CTTGGGCTTCTGGAACTTGG-3'
Myh10-F: 5'-GGAATCCTTTGGAAATGCGAAGA-3'
Myh10-R: 5'-GCCCCAACAATATAGCCAGTTAC-3'
Gapdh-F: 5'-CCCACTCTTCCACCTTCG-3'
Gapdh-R: 5'-TCCTTGGAGGCCATGTAG-3'

siRNA transfection

The following siRNAs were used to knock down specific genes. They were transfected into C2C12 cells using the Lipofectamine RNAiMax reagent (Thermo Fisher Scientific) following the manufacturer's instructions.

GFP (negative control): 5'-GCTGACCCTGAAGTTCATC-3'
Jak1: 5'-GCCTGAGAGTGGAGGTAAC-3'
Stat1: 5'-GGATCAAGTCATGTGCATA-3'
Atg5: 5'-GGCTCCTGGATTATGTCAT-3'

Microarray

Total mRNA were extracted from duplicated samples and subjected to microarray analysis using the Affymetrix GeneChip Mouse Genome 430 2.0 Array. The data were analysed by the GeneSpring software and deposited to GEO (Accession number: GSE262242).

Plasmid transfection

The Lipofectamine Transfection Reagent (Thermo Fisher Scientific) and the PLUS Reagent (Thermo Fisher Scientific) were used to transfect plasmids into C2C12 myoblasts following the manufacturer's instructions. Polyethylenimine (PEI, Polysciences) was used to transfect plasmids into HEK 293T cells.

Western blot

For cultured cells, Western blot was performed according to the standard procedures. For mouse tissues, the samples were homogenized using a T-25 digital IKA ULTRA-TURRAX disperser in a cell lysis buffer (25 mM Tris-HCl pH7.4, 150 mM NaCl, 1 mM EDTA, 1% NP-40, 5% glycerol) with a cocktail of protease inhibitors (20 mM p-nitrophenylphosphate, 20 mM β-glycerolphosphate, 0.5 mM phenylmethylsulfonyl fluoride, 2 μg/ml aprotinin, 0.5 μg/ml leupeptin, 0.7 μg/ml pepstatin, 50 μM sodium vanadate). The soluble lysates were used for Western blot. The primary antibodies used include anti-Jak1 (Upstate, 06–272), anti-Stat1 (Upstate, 06–501), anti-β-Tubulin (Sigma, T4026), anti-sarcomere myosin heavy chain (MHC) (DSHB, MF20), anti-GAPDH (Ambion, AM4300), anti-Myh9 (Cell Signaling, 3403), anti-Myh10 (Santa Cruz, sc-376942), anti-Flag (Sigma, F3165), and anti-HA (Roche, 12CA5). The Styxl2 antiserum was generated in-house by injecting rabbits with recombinant proteins spanning aa 2–142 of Styxl2 fused in-frame with glutathione S-transferase. The antiserum was purified with protein-G beads. The streptavidin-HRP was purchased from GE Healthcare (#RPN1231).

Immunostaining

C2C12 myoblasts were fixed with 4% paraformaldehyde (PFA) for 10 min at room temperature, and then washed with 0.1% PBST. Then samples were permeabilized with 0.5% PBST for 20 min. Zebrafishes were fixed with PFA for 2–4 hr at room temperature and washed with 0.1% PBST. Then the fishes were permeabilized with cold acetone for 8 min at –20 °C. The following procedures are the same for two types of samples. After permeabilization, the samples were washed with 0.1% PBST and blocked with 4% IgG-free BSA for 1 hr and then incubated with the primary antibody at 4 °C overnight. Then samples were washed with 0.1% PBST and incubated with the secondary antibody at room temperature for 1 hr. The DNA was stained with 100 ng/ml 4',6-diamidino-2-phenylindole (DAPI). For fish slow muscles, the nucleus was stained with an anti-Prox1 antibody. The primary antibodies used include anti-Flag (Sigma, F7425), anti-HA (Santa Cruz, sc-805), anti-α-Actinin (Sigma, A7732), anti-Prox1 (Angiobio, 11–002 P), anti-slow myosin heavy chain (DSHB, F59), anti-myosin heavy chain (DSHB, A4.1025), and anti-sarcomere myosin heavy chain (MHC) (DSHB, MF20).

Microinjection of zebrafish zygotes

The zygotes of zebrafish were collected in the morning. 2 nl of morpholino-containing solution was injected into fish zygotes as reported before (*Jin et al., 2009*). The concentration of morpholinos used for microinjection was 0.3~0.5 mM. A control morpholino targeting a non-related gene was used as negative control (Ctrl-MO). Morpholinos used were synthesized by Gene Tools (USA) and their sequences were listed below:

Ctrl-MO: 5'-AGCACACAAAGGCGAAGGTCAACAT-3'
Styxl2-MO: 5'-GCTGATCCTCCACAGACGACGCCAT-3'
Myh10-MO: 5'-CTTCACAAATGTGGTCTTACCTTGA-3'
Atg5-MO:5'-CACATCCTTGTCATCTGCCATTATC-3'

The DNA constructs of pCS2+-zStyxl2 (with several synonymous mutations near the start codon of zStyxl2 to make it MO-resistant) and pCS2+-zStyxl2ΔN493 were linearized and used as templates for in vitro transcription. The mRNA was synthesized using the mMESSAGE mMACHINE SP6 Kit (Ambion, AM1340) followed by purification with the MEGAclear Transcription Clean-Up Kit (Invitrogen, AM1908). The purified mRNA was dissolved in RNase-free water and diluted to 150 ng/µl immediately before microinjection.

Transmission electron microscopy

The heart and skeletal muscles were processed following the published protocols (*Graham and Orenstein, 2007*). Then the samples were examined by a Hitachi H7650 transmission electron microscope (Hitachi High-Technologies). The sarcomere length was measured from electron microscopic images with a magnification of 50,000 X. The length of 3–5 sarcomeres was measured for each mouse and a total of six mice were examined. The results were presented as mean ± SD. The unpaired Student's t-test was performed and $p < 0.05$ was considered statistically significant.

Measurement of muscle force generation in vitro

The gastrocnemius muscle of left hindlimb was carefully dissected from mice together with femur condyle and Achilles tendon. The twitch and tetanic force generated by the dissected gastrocnemius muscle and the muscle cross-sectional area (MCSA) were measured following published protocols (*Guo et al., 2016*). The force generated was recorded by the Dynamic Muscle Control system (DMC v5.4; Aurora Scientific) and analysed by the Dynamic Muscle Analysis system (DMA v3.2; Aurora Scientific). Both twitch and tetanic force were then normalized to the MCSA.

BioID and mass spectrometry

C2C12 myoblasts were infected by a retrovirus carrying pRetroX-Tet-On Advanced (kindly provided by Dr. Yusong Guo, the Hong Kong University of Science and Technology) and selected by 1 mg/ml G418 to get the Tet-on cells. Then the Tet-on cells were infected by a retrovirus carrying pTight-Styxl2-BirA*-HA and selected by 1.5 µg/ml puromycin to obtain stable Tet-Styxl2-BirA*-HA cells. Thus, the expression of Styxl2-BirA*-HA is controlled by the Tet-on system in these stable C2C12 myoblasts. These stable cells were seeded in GM and cultured for 24 hr before being induced to differentiate in DM for 48 hr. The medium was then replaced with DM containing 50 µM biotin (control) or 50 µM biotin plus 1 µg/ml doxycycline. After another 24 hr, the control and doxycycline-treated cells were processed for mass spectrometry analysis following the published protocols (*Roux et al., 2018*). Briefly, the biotinylated proteins were enriched by Dynabeads MyOne Streptavidin C1 (Invitrogen, #65001). The proteins bound to the beads were reduced with 10 mM Tris(2-carboxyethyl)phosphine hydrochloride (Sigma, C4706) at 40 °C for 30 min and alkylated with 20 mM Iodoacetamide (Sigma, I1149) in the dark for 30 min to prevent re-formation of the disulfide bond. The samples were digested with Trypsin Gold (Promega, V5280) overnight at 37 °C on a Thermomixer at 700 rpm followed by centrifugation. The supernatant was transferred to a new tube, acidified to pH2-3 by trifluoroacetic acid (Thermo Fisher, 85183), and desalted with a Pierce C18 spin column (Thermo Fisher Scientific, 89873). The tryptic peptides were labelled with iTRAQ reagents (AB Sciex, 4390812) following the manufacturer's instructions. Briefly, peptides from control cells were labelled with iTRAQ tag 114 and those from doxycycline-treated cells were labelled with tag 115. The labelled samples were mixed and fractionated by an UltiMate 3000 RSLCnano system (Thermo Fisher Scientific). A C18 Acclaim PepMap RSLC analytical column (75 µm×250 mm, 2 µm, 100 Å) with a C18 nano Viper trap-column (0.3 mm × 5 mm, Thermo Fisher Scientific) was used for peptide elution and separation at a flow rate of 300 nl/min. The mobile phase contained buffer A (0.1% formic acid, 2% acetonitrile) and B (0.1% formic acid, 98% acetonitrile). The gradient was set as follows: 0 min, 3% B; 10 min, 3% B; 12 min, 7% B; 62 min, 20% B; 64 min, 30% B; 65 min, 80% B; 73 min, 80% B; 73.1 min, 3% B; and 90 min, 3% B. MS data were then acquired using an Orbitrap Fusion Lumos mass spectrometer (Thermo Fisher Scientific) in a positive mode, with the following settings: (1) MS1 scan: 400–1600 m/z; resolution:

120,000; automatic gain control (AGC): 400,000; and maximum injection time: 50 ms; (2) The collision energy was set at 35% and orbitrap was used for MS2 scan as well; (3) MS2 scan starts from 100 m/z; resolution: 30,000; AGC: 50,000; and maximum injection time: 250 ms; (4) Exclusion window was set for 40 s; (5) The intensity threshold was set at 25,000. Data analysis was carried out using Mascot Deamon version 2.5.0 (Matrix Science) with standard settings for each instrument type and the data were searched against the *Mus musculus* database downloaded from SwissProt. A peptide tolerance of 10 ppm and fragment ion tolerance of 20 ppm were used. Carbamidomethylation of cysteine was specified as fixed modification, while oxidation of methionine and acetylation of protein N termini were set as variable modifications. The false discovery rate was set at 0.01 for proteins and peptide spectrum match. The 115/114 iTRAQ ratio of one protein was calculated based on the peak intensity of reporter ions by the software, and defined as Enrichment score for proteins in doxycycline-treated cells over that in control cells. The *p* values for each protein generated by the software were used for gene ontology analysis.

Gene ontology enrichment analysis

All the biotinylated proteins enriched (with Enrichment score >1) in cells expressing Styxl2-BirA*-HA were imported and analysed at Geneontology (http://geneontology.org/). The terms in the cellular component category were presented.

Immunoprecipitation

C2C12 cells or HEK293T cells were lysed in the lysis buffer with a cocktail of protease inhibitors. The soluble whole-cell lysates were first immunoprecipitated with an antibody targeting Styxl2, MEF2A (negative control), or Flag (Roche, F3165). The proteins co-precipitated were analysed by Western blot. In the ubiquitination assays, HEK 293T cells were lysed in the RIPA buffer (50 mM Tris-HCl, pH 7.4, 150 mM NaCl, 1 mM EDTA, 1% Triton X-100, 0.5% sodium deoxycholate, 0.1% SDS) with a cocktail of protease inhibitors and the soluble whole cell lysates were immunoprecipitated with an anti-Myc antibody (Santa Cruz, sc-40). The immunoprecipitated proteins were then analysed by Western blot.

Injury-induced muscle regeneration

Avertin was used to anaesthetize mice at 0.5 mg per gram of body weight by intraperitoneal injection. Then 120 µl (for females) or 150 µl (for males) of 10 µM Cardiotoxin was injected into muscles of each hind limb to induce acute injury. After >30 days, the muscles were dissected and tested. To examine protein levels at different time points, each tibialis anterior muscle was injected with 30 µl of 1.2% $BaCl_2$ to induce acute damage. The regenerating muscles were collected for Western blot at different time points.

Acknowledgements

Additional information

Author contributions

Xianwei Chen, Conceptualization, Data curation, Formal analysis, Investigation, Methodology, Writing - original draft, Writing - review and editing; Yanfeng Li, Conceptualization, Data curation, Formal analysis, Investigation, Methodology; Jin Xu, Yong Cui, Qian Wu, Haidi Yin, Yuying Li, Investigation, Methodology; Chuan Gao, Data curation, Formal analysis, Investigation, Methodology; Liwen Jiang, Huating Wang, Zilong Wen, Zhongping Yao, Supervision, Investigation, Methodology; Zhenguo Wu, Conceptualization, Data curation, Formal analysis, Supervision, Funding acquisition, Investigation, Methodology, Writing - original draft, Project administration, Writing - review and editing

Author ORCIDs

Xianwei Chen ⓘ http://orcid.org/0000-0002-5646-3245
Jin Xu ⓘ http://orcid.org/0000-0002-6840-1359
Huating Wang ⓘ http://orcid.org/0000-0001-5474-2905
Zhenguo Wu ⓘ http://orcid.org/0000-0003-3049-8324

Ethics

All animals were maintained and handled following the protocols approved by the Animal Ethics Committee of the Hong Kong University of Science and Technology.

Peer review material

Reviewer #1 (Public Review): https://doi.org/10.7554/eLife.87434.3.sa1
Reviewer #2 (Public Review): https://doi.org/10.7554/eLife.87434.3.sa2
Reviewer #3 (Public Review): https://doi.org/10.7554/eLife.87434.3.sa3
Author response https://doi.org/10.7554/eLife.87434.3.sa4

Additional files

Supplementary files
• MDAR checklist

Data availability

All data generated in this study are either included in the main figures and figure supplements or deposited to the Gene Expression Omnibus (accession number: GSE262242).Source data are also provided for the data presented in both main figures and figure supplements.

The following dataset was generated:

Author(s)	Year	Dataset title	Dataset URL	Database and Identifier
Chen X	2024	Profiling of transcriptional targets of Jak1 and Stat1 in proliferating and differentiating myoblasts	https://www.ncbi.nlm.nih.gov/geo/query/acc.cgi?acc=GSE262242	NCBI Gene Expression Omnibus, GSE262242

References

Alonso A, Sasin J, Bottini N, Friedberg I, Friedberg I, Osterman A, Godzik A, Hunter T, Dixon J, Mustelin T. 2004. Protein tyrosine phosphatases in the human genome. *Cell* **117**:699–711. DOI: https://doi.org/10.1016/j.cell.2004.05.018, PMID: 15186772

Arndt V, Dick N, Tawo R, Dreiseidler M, Wenzel D, Hesse M, Fürst DO, Saftig P, Saint R, Fleischmann BK, Hoch M, Höhfeld J. 2010. Chaperone-assisted selective autophagy is essential for muscle maintenance. *Current Biology* **20**:143–148. DOI: https://doi.org/10.1016/j.cub.2009.11.022, PMID: 20060297

Arrington CB, Bleyl SB, Matsunami N, Bonnell GD, Otterud BEM, Nielsen DC, Stevens J, Levy S, Leppert MF, Bowles NE. 2012. Exome analysis of a family with pleiotropic congenital heart disease. *Circulation. Cardiovascular Genetics* **5**:175–182. DOI: https://doi.org/10.1161/CIRCGENETICS.111.961797, PMID: 22337856

Avellaneda J, Rodier C, Daian F, Brouilly N, Rival T, Luis NM, Schnorrer F. 2021. Myofibril and mitochondria morphogenesis are coordinated by a mechanical feedback mechanism in muscle. *Nature Communications* **12**:2091. DOI: https://doi.org/10.1038/s41467-021-22058-7, PMID: 33828099

Azzedine H, Bolino A, Taïeb T, Birouk N, Di Duca M, Bouhouche A, Benamou S, Mrabet A, Hammadouche T, Chkili T, Gouider R, Ravazzolo R, Brice A, Laporte J, LeGuern E. 2003. Mutations in MTMR13, a new pseudophosphatase homologue of MTMR2 and Sbf1, in two families with an autosomal recessive demyelinating form of Charcot-Marie-Tooth disease associated with early-onset glaucoma. *American Journal of Human Genetics* **72**:1141–1153. DOI: https://doi.org/10.1086/375034, PMID: 12687498

Bellec Y, Harrar Y, Butaeye C, Darnet S, Bellini C, Faure JD. 2002. Pasticcino2 is a protein tyrosine phosphatase-like involved in cell proliferation and differentiation in Arabidopsis. *The Plant Journal* **32**:713–722. DOI: https://doi.org/10.1046/j.1365-313x.2002.01456.x, PMID: 12472687

Berger P, Berger I, Schaffitzel C, Tersar K, Volkmer B, Suter U. 2006. Multi-level regulation of myotubularin-related protein-2 phosphatase activity by myotubularin-related protein-13/set-binding factor-2. *Human Molecular Genetics* **15**:569–579. DOI: https://doi.org/10.1093/hmg/ddi473, PMID: 16399794

Bloor JW, Kiehart DP. 2001. zipper Nonmuscle myosin-II functions downstream of PS2 integrin in *Drosophila* myogenesis and is necessary for myofibril formation. *Developmental Biology* **239**:215–228. DOI: https://doi.org/10.1006/dbio.2001.0452, PMID: 11784030

Bogomolovas J, Fleming JR, Franke B, Manso B, Simon B, Gasch A, Markovic M, Brunner T, Knöll R, Chen J, Labeit S, Scheffner M, Peter C, Mayans O. 2021. Titin kinase ubiquitination aligns autophagy receptors with mechanical signals in the sarcomere. *EMBO Reports* **22**:e48018. DOI: https://doi.org/10.15252/embr.201948018, PMID: 34402565

Bönnemann CG, Laing NG. 2004. Myopathies resulting from mutations in sarcomeric proteins. *Current Opinion in Neurology* **17**:529–537. DOI: https://doi.org/10.1097/00019052-200410000-00003, PMID: 15367857

Chen MJ, Dixon JE, Manning G. 2017. Genomics and evolution of protein phosphatases. *Science Signaling* **10**:eaag1796. DOI: https://doi.org/10.1126/scisignal.aag1796, PMID: 28400531

Chen RH, Chen YH, Huang TY. 2019. Ubiquitin-mediated regulation of autophagy. *Journal of Biomedical Science* **26**:80. DOI: https://doi.org/10.1186/s12929-019-0569-y, PMID: 31630678

Cheng KCC, Klancer R, Singson A, Seydoux G. 2009. Regulation of MBK-2/DYRK by CDK-1 and the pseudophosphatases EGG-4 and EGG-5 during the oocyte-to-embryo transition. *Cell* **139**:560–572. DOI: https://doi.org/10.1016/j.cell.2009.08.047, PMID: 19879842

Chopra A, Kutys ML, Zhang K, Polacheck WJ, Sheng CC, Luu RJ, Eyckmans J, Hinson JT, Seidman JG, Seidman CE, Chen CS. 2018. Force generation via β-cardiac myosin, titin, and α-actinin drives cardiac sarcomere assembly from cell-matrix adhesions. *Developmental Cell* **44**:87–96. DOI: https://doi.org/10.1016/j.devcel.2017.12.012, PMID: 29316444

Clark KA, McElhinny AS, Beckerle MC, Gregorio CC. 2002. Striated muscle cytoarchitecture: an intricate web of form and function. *Annual Review of Cell and Developmental Biology* **18**:637–706. DOI: https://doi.org/10.1146/annurev.cellbio.18.012502.105840, PMID: 12142273

Conway SJ, Kruzynska-Frejtag A, Kneer PL, Machnicki M, Koushik SV. 2003. What cardiovascular defect does my prenatal mouse mutant have, and why? *Genesis* **35**:1–21. DOI: https://doi.org/10.1002/gene.10152, PMID: 12481294

Cooper LM, Waddell DS. 2020. A tale of two DUSP27s: proposed resolution for the naming of distinct dual-specificity phosphatases. *American Journal of Physiology. Cell Physiology* **319**:C148–C150. DOI: https://doi.org/10.1152/ajpcell.00201.2020, PMID: 32491926

Craig RW, Padrón R. 2004. Chapter 7 molecular structure of the sarcomere. Engel AC, Franzini-Armstrong C (Eds). *Myology*. McGraw-Hill. p. 129–166.

Da Costa M, Bach L, Landrieu I, Bellec Y, Catrice O, Brown S, De Veylder L, Lippens G, Inzé D, Faure JD. 2006. Arabidopsis PASTICCINO2 is an antiphosphatase involved in regulation of cyclin-dependent kinase A. *The Plant Cell* **18**:1426–1437. DOI: https://doi.org/10.1105/tpc.105.040485, PMID: 16698944

Das AT, Tenenbaum L, Berkhout B. 2016. Tet-on systems for doxycycline-inducible gene expression. *Current Gene Therapy* **16**:156–167. DOI: https://doi.org/10.2174/1566523216666160524144041, PMID: 27216914

Dlugosz AA, Antin PB, Nachmias VT, Holtzer H. 1984. The relationship between stress fiber-like structures and nascent myofibrils in cultured cardiac myocytes. *Journal of Cell Biology* **99**:2268–2278. DOI: https://doi.org/10.1083/jcb.99.6.2268, PMID: 6438115

Doyotte A, Mironov A, McKenzie E, Woodman P. 2008. The Bro1-related protein HD-PTP/PTPN23 is required for endosomal cargo sorting and multivesicular body morphogenesis. *PNAS* **105**:6308–6313. DOI: https://doi.org/10.1073/pnas.0707601105, PMID: 18434552

Dumont NA, Bentzinger CF, Sincennes MC, Rudnicki MA. 2015. Satellite cells and skeletal muscle regeneration. *Comprehensive Physiology* **5**:1027–1059. DOI: https://doi.org/10.1002/cphy.c140068, PMID: 26140708

Fenix AM, Neininger AC, Taneja N, Hyde K, Visetsouk MR, Garde RJ, Liu B, Nixon BR, Manalo AE, Becker JR, Crawley SW, Bader DM, Tyska MJ, Liu Q, Gutzman JH, Burnette DT. 2018. Muscle-specific stress fibers give rise to sarcomeres in cardiomyocytes. *eLife* **7**:e42144. DOI: https://doi.org/10.7554/eLife.42144, PMID: 30540249

Fero K, Bergeron SA, Horstick EJ, Codore H, Li GH, Ono F, Dowling JJ, Burgess HA. 2014. Impaired embryonic motility in dusp27 mutants reveals a developmental defect in myofibril structure. *Disease Models & Mechanisms* **7**:289–298. DOI: https://doi.org/10.1242/dmm.013235, PMID: 24203884

Firestein R, Nagy PL, Daly M, Huie P, Conti M, Cleary ML. 2002. Male infertility, impaired spermatogenesis, and azoospermia in mice deficient for the pseudophosphatase Sbf1. *The Journal of Clinical Investigation* **109**:1165–1172. DOI: https://doi.org/10.1172/JCI12589, PMID: 11994405

Friedberg I, Nika K, Tautz L, Saito K, Cerignoli F, Friedberg I, Godzik A, Mustelin T. 2007. Identification and characterization of DUSP27, a novel dual-specific protein phosphatase. *FEBS Letters* **581**:2527–2533. DOI: https://doi.org/10.1016/j.febslet.2007.04.059, PMID: 17498703

Graham L, Orenstein JM. 2007. Processing tissue and cells for transmission electron microscopy in diagnostic pathology and research. *Nature Protocols* **2**:2439–2450. DOI: https://doi.org/10.1038/nprot.2007.304, PMID: 17947985

Guo A, Leung K, Qin J, Chow SK, Cheung W. 2016. Effect of low-magnitude, high-frequency vibration treatment on retardation of sarcopenia: senescence-accelerated mouse-p8 model. *Rejuvenation Research* **19**:293–302. DOI: https://doi.org/10.1089/rej.2015.1759

Gutzman JH, Sahu SU, Kwas C. 2015. Non-muscle myosin IIA and IIB differentially regulate cell shape changes during zebrafish brain morphogenesis. *Developmental Biology* **397**:103–115. DOI: https://doi.org/10.1016/j.ydbio.2014.10.017, PMID: 25446029

Hasty P, Bradley A, Morris JH, Edmondson DG, Venuti JM, Olson EN, Klein WH. 1993. Muscle deficiency and neonatal death in mice with a targeted mutation in the myogenin gene. *Nature* **364**:501–506. DOI: https://doi.org/10.1038/364501a0, PMID: 8393145

Hinton SD, Myers MP, Roggero VR, Allison LA, Tonks NK. 2010. The pseudophosphatase MK-STYX interacts with G3BP and decreases stress granule formation. *The Biochemical Journal* **427**:349–357. DOI: https://doi.org/10.1042/BJ20091383, PMID: 20180778

Hinton SD. 2019. The role of pseudophosphatases as signaling regulators. *Biochimica et Biophysica Acta (BBA) - Molecular Cell Research* **1866**:167–174. DOI: https://doi.org/10.1016/j.bbamcr.2018.07.021

Hinton SD. 2020. Pseudophosphatase MK-STYX: the atypical member of the MAP kinase phosphatases. *The FEBS Journal* **287**:4221–4231. DOI: https://doi.org/10.1111/febs.15426, PMID: 32472731

Holtzer H, Hijikata T, Lin ZX, Zhang ZQ, Holtzer S, Protasi F, Franzini-Armstrong C, Sweeney HL. 1997. Independent assembly of 1.6 microns long bipolar MHC filaments and I-Z-I bodies. *Cell Structure and Function* **22**:83–93. DOI: https://doi.org/10.1247/csf.22.83, PMID: 9113394

Jin H, Sood R, Xu J, Zhen F, English MA, Liu PP, Wen Z. 2009. Definitive hematopoietic stem/progenitor cells manifest distinct differentiation output in the zebrafish VDA and PBI. *Development* **136**:647–654. DOI: https://doi.org/10.1242/dev.029637, PMID: 19168679

Keller C, Hansen MS, Coffin CM, Capecchi MR. 2004. Pax3:Fkhr interferes with embryonic Pax3 and Pax7 function: implications for alveolar rhabdomyosarcoma cell of origin. *Genes & Development* **18**:2608–2613. DOI: https://doi.org/10.1101/gad.1243904, PMID: 15520281

Kharitidi D, Manteghi S, Pause A. 2014. Pseudophosphatases: methods of analysis and physiological functions. *Methods* **65**:207–218. DOI: https://doi.org/10.1016/j.ymeth.2013.09.009, PMID: 24064037

Kharitidi D, Apaja PM, Manteghi S, Suzuki K, Malitskaya E, Roldan A, Gingras MC, Takagi J, Lukacs GL, Pause A. 2015. Interplay of endosomal ph and ligand occupancy in integrin α5β1 ubiquitination. *Endocytic Sorting, and Cell Migration. Cell Reports* **13**:599–609. DOI: https://doi.org/10.1016/j.celrep.2015.09.024

Kirkin V, McEwan DG, Novak I, Dikic I. 2009. A role for ubiquitin in selective autophagy. *Molecular Cell* **34**:259–269. DOI: https://doi.org/10.1016/j.molcel.2009.04.026, PMID: 19450525

Lakso M, Pichel JG, Gorman JR, Sauer B, Okamoto Y, Lee E, Alt FW, Westphal H. 1996. Efficient in vivo manipulation of mouse genomic sequences at the zygote stage. *PNAS* **93**:5860–5865. DOI: https://doi.org/10.1073/pnas.93.12.5860, PMID: 8650183

Livak KJ, Schmittgen TD. 2001. Analysis of relative gene expression data using real-time quantitative PCR and the 2(-Delta Delta C(T)) Method. *Methods* **25**:402–408. DOI: https://doi.org/10.1006/meth.2001.1262, PMID: 11846609

Loison O, Weitkunat M, Kaya-Çopur A, Nascimento Alves C, Matzat T, Spletter ML, Luschnig S, Brasselet S, Lenne PF, Schnorrer F. 2018. Polarization-resolved microscopy reveals a muscle myosin motor-independent mechanism of molecular actin ordering during sarcomere maturation. *PLOS Biology* **16**:e2004718. DOI: https://doi.org/10.1371/journal.pbio.2004718, PMID: 29702642

Lu MH, DiLullo C, Schultheiss T, Holtzer S, Murray JM, Choi J, Fischman DA, Holtzer H. 1992. The vinculin/sarcomeric-alpha-actinin/alpha-actin nexus in cultured cardiac myocytes. *The Journal of Cell Biology* **117**:1007–1022. DOI: https://doi.org/10.1083/jcb.117.5.1007, PMID: 1577864

Luis NM, Schnorrer F. 2021. Mechanobiology of muscle and myofibril morphogenesis. *Cells & Development* **168**:203760. DOI: https://doi.org/10.1016/j.cdev.2021.203760

Ma X, Takeda K, Singh A, Yu ZX, Zerfas P, Blount A, Liu C, Towbin JA, Schneider MD, Adelstein RS, Wei Q. 2009. Conditional ablation of nonmuscle myosin II-B delineates heart defects in adult mice. *Circulation Research* **105**:1102–1109. DOI: https://doi.org/10.1161/CIRCRESAHA.109.200303, PMID: 19815823

Ma H, Wardega P, Mazaud D, Klosowska-Wardega A, Jurek A, Engström U, Lennartsson J, Heldin CH. 2015. Histidine-domain-containing protein tyrosine phosphatase regulates platelet-derived growth factor receptor intracellular sorting and degradation. *Cellular Signalling* **27**:2209–2219. DOI: https://doi.org/10.1016/j.cellsig.2015.07.020, PMID: 26232618

Mao Q, Acharya A, Rodríguez-delaRosa A, Marchiano F, Dehapiot B, Al Tanoury Z, Rao J, Díaz-Cuadros M, Mansur A, Wagner E, Chardes C, Gupta V, Lenne PF, Habermann BH, Theodoly O, Pourquié O, Schnorrer F. 2022. Tension-driven multi-scale self-organisation in human iPSC-derived muscle fibers. *eLife* **11**:e76649. DOI: https://doi.org/10.7554/eLife.76649, PMID: 35920628

Martin TG, Kirk JA. 2020. Under construction: The dynamic assembly, maintenance, and degradation of the cardiac sarcomere. *Journal of Molecular and Cellular Cardiology* **148**:89–102. DOI: https://doi.org/10.1016/j.yjmcc.2020.08.018, PMID: 32920010

Maruyama R, Velarde NV, Klancer R, Gordon S, Kadandale P, Parry JM, Hang JS, Rubin J, Stewart-Michaelis A, Schweinsberg P, Grant BD, Piano F, Sugimoto A, Singson A. 2007. EGG-3 regulates cell-surface and cortex rearrangements during EGG activation in *Caenorhabditis elegans*. *Current Biology* **17**:1555–1560. DOI: https://doi.org/10.1016/j.cub.2007.08.011, PMID: 17869112

Masiero E, Agatea L, Mammucari C, Blaauw B, Loro E, Komatsu M, Metzger D, Reggiani C, Schiaffino S, Sandri M. 2009. Autophagy is required to maintain muscle mass. *Cell Metabolism* **10**:507–515. DOI: https://doi.org/10.1016/j.cmet.2009.10.008, PMID: 19945408

McCarthy JJ, Srikuea R, Kirby TJ, Peterson CA, Esser KA. 2012. Inducible Cre transgenic mouse strain for skeletal muscle-specific gene targeting. *Skeletal Muscle* **2**:8. DOI: https://doi.org/10.1186/2044-5040-2-8, PMID: 22564549

Mizushima N, Yoshimori T, Levine B. 2010. Methods in mammalian autophagy research. *Cell* **140**:313–326. DOI: https://doi.org/10.1016/j.cell.2010.01.028, PMID: 20144757

Mukund K, Subramaniam S. 2020. Skeletal muscle: a review of molecular structure and function, in health and disease. *Wiley Interdisciplinary Reviews. Systems Biology and Medicine* **12**:e1462. DOI: https://doi.org/10.1002/wsbm.1462, PMID: 31407867

Murphy MM, Lawson JA, Mathew SJ, Hutcheson DA, Kardon G. 2011. Satellite cells, connective tissue fibroblasts and their interactions are crucial for muscle regeneration. *Development* **138**:3625–3637. DOI: https://doi.org/10.1242/dev.064162, PMID: 21828091

Nakai A, Yamaguchi O, Takeda T, Higuchi Y, Hikoso S, Taniike M, Omiya S, Mizote I, Matsumura Y, Asahi M, Nishida K, Hori M, Mizushima N, Otsu K. 2007. The role of autophagy in cardiomyocytes in the basal state and in response to hemodynamic stress. *Nature Medicine* **13**:619–624. DOI: https://doi.org/10.1038/nm1574, PMID: 17450150

Nakhro K, Park JM, Hong YB, Park JH, Nam SH, Yoon BR, Yoo JH, Koo H, Jung SC, Kim HL, Kim JY, Choi KG, Choi BO, Chung KW. 2013. SET binding factor 1 (SBF1) mutation causes Charcot-Marie-Tooth disease type 4B3. *Neurology* **81**:165–173. DOI: https://doi.org/10.1212/WNL.0b013e31829a3421, PMID: 23749797

Nandi D, Tahiliani P, Kumar A, Chandu D. 2006. The ubiquitin-proteasome system. *Journal of Biosciences* **31**:137–155. DOI: https://doi.org/10.1007/BF02705243, PMID: 16595883

Newell-Litwa KA, Horwitz R, Lamers ML. 2015. Non-muscle myosin II in disease: mechanisms and therapeutic opportunities. *Disease Models & Mechanisms* **8**:1495–1515. DOI: https://doi.org/10.1242/dmm.022103, PMID: 26542704

Pankiv S, Clausen TH, Lamark T, Brech A, Bruun JA, Outzen H, Øvervatn A, Bjørkøy G, Johansen T. 2007. p62/SQSTM1 binds directly to Atg8/LC3 to facilitate degradation of ubiquitinated protein aggregates by autophagy. *The Journal of Biological Chemistry* **282**:24131–24145. DOI: https://doi.org/10.1074/jbc.M702824200, PMID: 17580304

Parker F, Baboolal TG, Peckham M. 2020. Actin mutations and their role in disease. *International Journal of Molecular Sciences* **21**:3371. DOI: https://doi.org/10.3390/ijms21093371, PMID: 32397632

Parker F, Peckham M. 2020. Disease mutations in striated muscle myosins. *Biophysical Reviews* **12**:887–894. DOI: https://doi.org/10.1007/s12551-020-00721-5, PMID: 32651905

Parkinson MDJ, Piper SC, Bright NA, Evans JL, Boname JM, Bowers K, Lehner PJ, Luzio JP. 2015. A non-canonical ESCRT pathway, including histidine domain phosphotyrosine phosphatase (HD-PTP), is used for down-regulation of virally ubiquitinated MHC class I. *The Biochemical Journal* **471**:79–88. DOI: https://doi.org/10.1042/BJ20150336, PMID: 26221024

Radhakrishna U, Albayrak S, Alpay-Savasan Z, Zeb A, Turkoglu O, Sobolewski P, Bahado-Singh RO. 2016. Genome-wide dna methylation analysis and epigenetic variations associated with congenital aortic valve stenosis (AVS). *PLOS ONE* **11**:e0154010. DOI: https://doi.org/10.1371/journal.pone.0154010, PMID: 27152866

Reiterer V, Fey D, Kolch W, Kholodenko BN, Farhan H. 2013. Pseudophosphatase STYX modulates cell-fate decisions and cell migration by spatiotemporal regulation of ERK1/2. *PNAS* **110**:E2934–E2943. DOI: https://doi.org/10.1073/pnas.1301985110, PMID: 23847209

Reiterer V, Pawłowski K, Farhan H. 2017. STYX: a versatile pseudophosphatase. *Biochemical Society Transactions* **45**:449–456. DOI: https://doi.org/10.1042/BST20160279, PMID: 28408485

Reiterer V, Pawłowski K, Desrochers G, Pause A, Sharpe HJ, Farhan H. 2020. The dead phosphatases society: a review of the emerging roles of pseudophosphatases. *The FEBS Journal* **287**:4198–4220. DOI: https://doi.org/10.1111/febs.15431, PMID: 32484316

Rhee D, Sanger JM, Sanger JW. 1994. The premyofibril: evidence for its role in myofibrillogenesis. *Cell Motility* **28**:1–24. DOI: https://doi.org/10.1002/cm.970280102

Robinson FL, Dixon JE. 2005. The phosphoinositide-3-phosphatase MTMR2 associates with MTMR13, a membrane-associated pseudophosphatase also mutated in type 4B Charcot-Marie-Tooth disease. *The Journal of Biological Chemistry* **280**:31699–31707. DOI: https://doi.org/10.1074/jbc.M505159200, PMID: 15998640

Roux KJ, Kim DI, Raida M, Burke B. 2012. A promiscuous biotin ligase fusion protein identifies proximal and interacting proteins in mammalian cells. *The Journal of Cell Biology* **196**:801–810. DOI: https://doi.org/10.1083/jcb.201112098, PMID: 22412018

Roux KJ, Kim DI, Burke B, May DG. 2018. BioID: a screen for protein-protein interactions. *Current Protocols in Protein Science* **91**:19. DOI: https://doi.org/10.1002/cpps.51, PMID: 29516480

Rudnicki MA, Schnegelsberg PN, Stead RH, Braun T, Arnold HH, Jaenisch R. 1993. MyoD or Myf-5 is required for the formation of skeletal muscle. *Cell* **75**:1351–1359. DOI: https://doi.org/10.1016/0092-8674(93)90621-v, PMID: 8269513

Rui Y, Bai J, Perrimon N. 2010. Sarcomere formation occurs by the assembly of multiple latent protein complexes. *PLOS Genetics* **6**:e1001208. DOI: https://doi.org/10.1371/journal.pgen.1001208, PMID: 21124995

Sanger JW, Kang S, Siebrands CC, Freeman N, Du A, Wang J, Stout AL, Sanger JM. 2006. How to build a myofibril. *Journal of Muscle Research and Cell Motility* **26**:343–354. DOI: https://doi.org/10.1007/s10974-005-9016-7

Sanger JW, Wang J, Holloway B, Du A, Sanger JM. 2009. Myofibrillogenesis in skeletal muscle cells in zebrafish. *Cell Motility and the Cytoskeleton* **66**:556–566. DOI: https://doi.org/10.1002/cm.20365, PMID: 19382198

Sanger JW, Wang J, Fan Y, White J, Mi-Mi L, Dube DK, Sanger JM, Pruyne D. 2017. Assembly and maintenance of myofibrils in Striated muscle. Sanger JW, Wang J (Eds). *Handbook of Experimental Pharmacology*. Elsevier. p. 39–75. DOI: https://doi.org/10.1007/164_2016_53, PMID: 27832381

Schwander M, Leu M, Stumm M, Dorchies OM, Ruegg UT, Schittny J, Müller U. 2003. Beta1 integrins regulate myoblast fusion and sarcomere assembly. *Developmental Cell* **4**:673–685. DOI: https://doi.org/10.1016/s1534-5807(03)00118-7, PMID: 12737803

Shaid S, Brandts CH, Serve H, Dikic I. 2013. Ubiquitination and selective autophagy. *Cell Death and Differentiation* **20**:21–30. DOI: https://doi.org/10.1038/cdd.2012.72, PMID: 22722335

Sparrow JC, Schöck F. 2009. The initial steps of myofibril assembly: integrins pave the way. *Nature Reviews. Molecular Cell Biology* **10**:293–298. DOI: https://doi.org/10.1038/nrm2634, PMID: 19190670

Squire JM. 2005. Molecular architecture in muscle contractile assemblies in advances in protein chemistry. *Academic Press* **71**:17–87. DOI: https://doi.org/10.1016/S0065-3233(04)71002-5

Sun L, Ma K, Wang H, Xiao F, Gao Y, Zhang W, Wang K, Gao X, Ip N, Wu Z. 2007. JAK1-STAT1-STAT3, a key pathway promoting proliferation and preventing premature differentiation of myoblasts. *The Journal of Cell Biology* **179**:129–138. DOI: https://doi.org/10.1083/jcb.200703184, PMID: 17908914

Tallquist MD, Weismann KE, Hellström M, Soriano P. 2000. Early myotome specification regulates PDGFA expression and axial skeleton development. *Development* **127**:5059–5070. DOI: https://doi.org/10.1242/dev.127.23.5059, PMID: 11060232

Tomar VS, Baral TK, Nagavelu K, Somasundaram K. 2019. Serine/threonine/tyrosine-interacting-like protein 1 (STYXL1), a pseudo phosphatase, promotes oncogenesis in glioma. *Biochemical and Biophysical Research Communications* **515**:241–247. DOI: https://doi.org/10.1016/j.bbrc.2019.05.093, PMID: 31146910

Tonks NK. 2006. Protein tyrosine phosphatases: from genes, to function, to disease. *Nature Reviews. Molecular Cell Biology* **7**:833–846. DOI: https://doi.org/10.1038/nrm2039, PMID: 17057753

Tullio AN, Accili D, Ferrans VJ, Yu ZX, Takeda K, Grinberg A, Westphal H, Preston YA, Adelstein RS. 1997. Nonmuscle myosin II-B is required for normal development of the mouse heart. *PNAS* **94**:12407–12412. DOI: https://doi.org/10.1073/pnas.94.23.12407, PMID: 9356462

Wang J, Fan Y, Sanger JM, Sanger JW. 2018. Nonmuscle myosin II in cardiac and skeletal muscle cells. *Cytoskeleton* **75**:339–351. DOI: https://doi.org/10.1002/cm.21454, PMID: 29781105

Weinfeld M, Mani RS, Abdou I, Aceytuno RD, Glover JNM. 2011. Tidying up loose ends: the role of polynucleotide kinase/phosphatase in DNA strand break repair. *Trends in Biochemical Sciences* **36**:262–271. DOI: https://doi.org/10.1016/j.tibs.2011.01.006, PMID: 21353781

Weitkunat M, Kaya-Çopur A, Grill SW, Schnorrer F. 2014. Tension and force-resistant attachment are essential for myofibrillogenesis in *Drosophila* flight muscle. *Current Biology* **24**:705–716. DOI: https://doi.org/10.1016/j.cub.2014.02.032, PMID: 24631244

White J, Barro MV, Makarenkova HP, Sanger JW, Sanger JM. 2014. Localization of sarcomeric proteins during myofibril assembly in cultured mouse primary skeletal myotubes. *Anatomical Record* **297**:1571–1584. DOI: https://doi.org/10.1002/ar.22981, PMID: 25125171

White J, Wang J, Fan Y, Dube DK, Sanger JW, Sanger JM. 2018. Myofibril assembly in cultured mouse neonatal cardiomyocytes. *The Anatomical Record* **301**:2067–2079. DOI: https://doi.org/10.1002/ar.23961

Wiese S, Reidegeld KA, Meyer HE, Warscheid B. 2007. Protein labeling by iTRAQ: a new tool for quantitative mass spectrometry in proteome research. *Proteomics* **7**:340–350. DOI: https://doi.org/10.1002/pmic.200600422, PMID: 17177251

Wishart MJ, Denu JM, Williams JA, Dixon JE. 1995. A single mutation converts: A novel phosphotyrosine binding domain into A dual-specificity phosphatase. *The Journal of Biological Chemistry* **270**:26782–26785. DOI: https://doi.org/10.1074/jbc.270.45.26782, PMID: 7592916

Wishart MJ, Dixon JE. 2002. The archetype STYX/dead-phosphatase complexes with a spermatid mRNA-binding protein and is essential for normal sperm production. *PNAS* **99**:2112–2117. DOI: https://doi.org/10.1073/pnas.251686198, PMID: 11842224

Worby CA, Gentry MS, Dixon JE. 2006. Laforin, a dual specificity phosphatase that dephosphorylates complex carbohydrates. *The Journal of Biological Chemistry* **281**:30412–30418. DOI: https://doi.org/10.1074/jbc.M606117200, PMID: 16901901

Xiao F, Wang H, Fu X, Li Y, Ma K, Sun L, Gao X, Wu Z. 2011. Oncostatin M inhibits myoblast differentiation and regulates muscle regeneration. *Cell Research* **21**:350–364. DOI: https://doi.org/10.1038/cr.2010.144, PMID: 20956996

Yamamoto Y, Chino H, Tsukamoto S, Ode KL, Ueda HR, Mizushima N. 2021. NEK9 regulates primary cilia formation by acting as a selective autophagy adaptor for MYH9/myosin IIA. *Nature Communications* **12**:3292. DOI: https://doi.org/10.1038/s41467-021-23599-7, PMID: 34078910

Zaffagnini G, Martens S. 2016. Mechanisms of selective autophagy. *Journal of Molecular Biology* **428**:1714–1724. DOI: https://doi.org/10.1016/j.jmb.2016.02.004, PMID: 26876603